Journal of Power Sources 581 (2023) 233449

Contents lists available at ScienceDirect

Journal of Power Sources

journal homepage: www.elsevier.com/locate/jpowsour

Experimental identification of the impact of direct internal and external methane reforming on SOFC by detailed online monitoring and supporting measurements

Michael Höber [a,*], Benjamin Königshofer [a], Hartmuth Schröttner [b,c], Harald Fitzek [c], Norbert H. Menzler [d], Christoph Hochenauer [a], Vanja Subotić [a]

[a] Institute of Thermal Engineering, Graz University of Technology, Inffeldgasse 25/B, 8010 Graz, Austria
[b] Institute of Electron Microscopy and Nanoanalysis (FELMI), Graz University of Technology, Steyrergasse 17, 8010 Graz, Austria
[c] Graz Centre for Electron Microscopy (ZFE), Steyrergasse 17, 8010 Graz, Austria
[d] Institute of Energy and Climate Research (IEK), IEK-1: Materials Synthesis and Processing, Forschungszentrum Jülich GmbH, Wilhelm-Johnen-Str., Jülich, 52425, Germany

HIGHLIGHTS

- Impact of internal and external reformed methane on industrial size single SOFC.
- The effect of flow rate and operating temperature variation is investigated.
- Temporary increasing ohmic resistance due to direct internal reforming is observed.
- Internal methane reforming can accelerate structural changes of the air electrode.

ARTICLE INFO

Keywords:
Solid Oxide Fuel Cell (SOFC)
Methane reforming
Online monitoring
Electrochemical analysis

ABSTRACT

Solid Oxide Fuel Cells (SOFCs) are able to use biogas or natural gas with its main compound methane as fuel but utilization of methane bears risks which can lead to early performance loss. Application of a suitable type of methane reforming as well as online monitoring tools and a holistic knowledge about possible degradation mechanisms can limit degradation rates. Here, we compare direct internal reforming and external methane reforming on a large planar SOFC with an active area of 80 cm^2 at different operating temperatures and methane flow rates. To do so, the measured temperature distribution, applied electrochemical impedance spectroscopy and its advanced tool distribution of relaxation times (DRT) as well as results from post mortem microscopic analysis are used. We observed that the ohmic resistance and high frequency peaks in the DRT spectra seem to be influenced not only by the average cell temperature but also by direct internal reforming (DIR) conditions. Furthermore, we observed that high temperature gradients induced by DIR could lead to or accelerate damages of the cells structure and the sealing. The results presented in this work are useful to control or manage safe SOFC operation with C containing fuels for real world SOFC applications.

1. Introduction

Reducing greenhouse gas emissions and minimizing the consumption of fossil fuels while establishing a stable on demand power supply is one of the major challenges of today's society. One sector, which relies heavily on fossil fuels but is essential for the modern society is the agro industry. The agro industry is responsible for more than 10% of greenhouse gas emissions within the European Union (EU) [1]. One example of energy intensive cultivation is the cultivation of tomatoes in greenhouses. To compensate parts of the energy needed for tomato cultivation, the waste biomass could be used to generate the needed energy. Tomato cultivation is expected to produce 15 tons of waste biomass per hectare and year. The 15 tons of waste biomass can be turned into biogas for energy production which results in a potential heating value of approximately 33 GJ per hectare and year if only methane is used from the produced biogas [2,3].

One possible high efficient energy converter which is capable of utilizing methane, biogas or gasified biomass nearly without pre-treatment

---

* Corresponding author.
E-mail address: michael.hoeber@tugraz.at (M. Höber).

https://doi.org/10.1016/j.jpowsour.2023.233449
Received 28 April 2023; Received in revised form 17 July 2023; Accepted 19 July 2023

is a solid oxide fuel cell (SOFC) system [4–7]. SOFCs are able to electrochemically oxidize both H_2 and CO which are products of reformed methane and biogas. The highly efficient manner and the use of biogas enable environmentally friendly operation. The high fuel flexibility of SOFCs is enhanced by their ability to directly reform methane mixed with steam or CO_2 into H_2 and CO at the fuel electrode of the SOFC [8–11]. Latter leads to a combination of high electrical efficiencies [12] and high fuel flexibility [13]. However, for both reforming types, mixtures of carbonaceous gases such as CH_4, CO and CO_2 and H_2O might be present at the fuel cells anode. That includes the risk of performance loss caused by (i) carbon deposition [4,9,14–21], (ii) Ni re-oxidation [4,9,22–24], (iii) fuel contaminants such as H_2S and HCl which are often found in carbonaceous gases [25–27] or (iv) breaking of the cell or its sealing due to thermal stresses caused by a mixture of chemical and electrochemical reactions at the fuel electrode [28–30]. A detailed summary of the impact of different fuels and impurities on SOFC operation can be found in [31]. Some of the previous listed causes for performance loss might be limited and the lifetime could be expanded if they are detected at an early stage and countermeasures are initiated. To observe performance loss of electrochemical cells in situ, online monitoring measurements such as electrochemical impedance spectroscopy (EIS) and its advanced tool distribution of relaxation times (DRT) can be applied. EIS measurements can be used for performance characterization but also to provide insight into complex mechanisms such as carbon deposition [11,32–34]. Ni re-oxidation [17,24] and other degradation mechanisms, such as electrode delamination [29], can also be observed applying EIS. It is possible to detect all these different kinds of degradation because EIS measurements show process losses which arise during operation of the electrochemical cell. Online monitoring by EIS measurements can be used for a wide field of application, from fuel cells [35] and batteries [36] even to catalysts [37–40]. However, the interpretation of EIS and DRT spectra relies on previous conducted experiments and a detailed understanding of the causation of degradation which is significantly enhanced within this study. This knowledge gained enables to develop appropriate counteractions and to prolong the lifetime of SOFCs. However, a large database of experiments is needed to interpret and use measured EIS and DRT spectra to optimize real world applications. Applying knowledge of EIS measurement could be used for example to define accelerated degradation conditions to predict long term degradation [41]. To gain knowledge of appearing losses caused by using direct internal reforming (DIR) of methane and externally reformed methane, different cells and cell sizes were tested in literature. Testing of a 10×10 mm^2 cell showed that at least one loss process (one peak in the DRT spectra) is related to internal reforming [42]. In addition to reforming directly on the fuel electrode, it was also found, that the Ni-mesh on the fuel electrode side has a non-negligible catalytic effect [43]. Caliandro et al. tested cells with a diameter up to 60 mm and found dependencies of loss processes (peaks in the DRT spectra) on the type of methane reforming but no temperature distributions were measured for confirmation [10]. A comparison of direct internal steam and dry reforming showed a dependency of several peaks in the DRT spectra on the methane reforming type and steam to carbon ratios (H_2O/C) but also no temperature distribution measurements were conducted for further interpretation [11]. The combination of changing operating temperature, volume flows and gas compositions in combination with EIS, DRT and temperature distribution measurements for a more holistic testing, as done in this work, can still contribute to literature. The spatially distributed temperature measurements along the cell could give information about chemical and electrochemical reaction zones along the cell which might be linked to losses observed. A selection of the endo- and exothermal reactions which are likely to be observed when SOFCs are fueled with methane mixtures are summarized in Table 1. Several other reactions and reaction paths might occur as shown in [44] but are not listed here for the sake of conciseness.

As seen in Table 1, methane reforming reactions such as steam reforming (1) and dry reforming (2) are endothermal reactions while electrochemical oxidation reactions of H_2 (4) and CO (5) as well as the water gas shift reaction (3) are exothermal. Hence, high temperature gradients are possible for DIR of methane, especially for large, industrial relevant sized, cells as tested in this work. The temperature gradients might influence the degradation and losses arising in the cell. Furthermore, thermal stresses can directly cause damages of the cell, which can be avoided if temperature gradients are limited to less than 10 K cm^{-1}, as stated in [45]. To observe the impact of the temperature gradients, large cells or stacks with flow fields and sizes such as in real world application are required.

We tested a large planar SOFC with an active area of 80 cm^2, which is also used in stacks [46], with three different H_2O/C ratios at three different temperatures and two different methane flow rates for direct internally reformed and externally auto-thermal reformed gas compositions. This was done to identify trends in the temperature distributions and online monitoring results caused by the reforming reactions and utilization of methane. A detailed temperature distribution along the industrial sized SOFC is monitored with 12 thermocouples. This detailed temperature field gives insight into possible thermal stresses and locations of the endo- and exothermal reforming reactions. The measured temperature distribution provides necessary information for further interpretation of the measured EIS and calculated DRT spectra. The combination of EIS measurements, application of the DRT method, detailed temperature monitoring, an industrial relevant size of the cell and the variation of fuel flows, reforming types for methane and operating temperature shown in this paper contribute to the overall knowledge to find and identify suitable operating conditions for methane operated SOFCs and enhance their lifetime.

The trends and results shown in this work might help to identify the type or nature of changes which occur during operation of SOFC systems with either direct internal reforming conditions or with an external reformer upstream of the SOFC. Further, the measured temperature gradients along the cell under different conditions could help to validate simulation models, choose the right operating parameter or choose the suitable type of reforming for the development of SOFC systems.

2. Experimental

This section explains the experimental setup and data processing applied in this study. The SOFC and the used test rig are described in the first part. The second part is about the test procedure and the applied test matrix. In the third part, the post-processing methodology of the measurement data and the approach to calculate the DRT spectra is shown.

2.1. Large planar single cell test rig

A commercial large planar anode supported cell (ASC) with a total area of 10×10 cm^2 and an active area of 80 cm^2 is used within this study. The industrial relevant size of the cell is necessary to observe reaction zones via temperature distributions and the influence of chemical and electrochemical reactions on the cell performance. The ASC consists of a 350 μm thick Ni/8 YSZ (Yttria-stabilized Zirconia) fuel electrode substrate, an 8 μm thick real fuel electrode (anode) composed also of Ni/8 YSZ, an 8 YSZ electrolyte, a Gadolinium doped Ceria (GDC) barrier layer between electrolyte and air electrode and a Lanthanum Strontium Cobalt Ferrite (LSCF) (La0.58Sr0.4Co0.2Fe0.8O3-delta) air electrode. The total thickness of the cell is about 393 μm, more detailed information can be found in [47]. Stable long-term performance of the cell type has already been proven in [46].

The test rig used within this work consists of a gas supply and mixing unit, an in-house developed steam generator, compressed air supply, an electric furnace where the ceramic cell housing, made from

Table 1
Selected reactions that occur during the utilization of methane in the SOFC [11,44].

Name	Equation	Molar enthalpy in kJ mol^{-1} 750 °C	Number
CH_4 steam reforming	$CH_4 + H_2O \rightarrow 3\ H_2 + CO$	224.8	(1)
CH_4 dry reforming	$CH_4 + CO_2 \rightarrow 2\ H_2 + 2\ CO$	259.5	(2)
Water gas shift reaction	$CO + H_2O \rightarrow CO_2 + H_2$	−34.6	(3)
Electrochemical oxidation of H_2	$H_2 + O^{2-} \rightarrow H_2O + 2\ e^-$	−247.9	(4)
Electrochemical oxidation of CO	$CO + O^{2-} \rightarrow CO_2 + 2\ e^-$	−282.5	(5)
CH_4 cracking	$CH_4 \rightarrow C + 2\ H_2$	97.7	(6)
Boudouard reaction	$C + CO_2 \rightarrow 2\ CO$	161.7	(7)
Carbon steam gasification	$C + H_2O \rightarrow CO + H_2$	135.8	(8)

alumina, is placed and an electric load. Used gases are stored in bottles and their flow rates are controlled by mass flow controllers (MFCs) purchased from Voegtlin Instruments GmbH. Detailed information about the used gases can be found in [48]. The steam flow rate is controlled by a flow regulated pump (AZURA P 2.1S) purchased from Knauer Wissenschaftliche Geräte GmbH. On the air electrode side, compressed air flows through a three stage filter system and the flow rate is also controlled by a MFC. Within this work, the cell is operated in co-flow configuration. The SOFC is contacted with a Ni-mesh and Pt wires at the fuel electrode and a Pt-mesh and Pt wires at the air electrode. A Ni-mesh is used on the fuel electrode side since Pt is expensive and can form alloys with Ni, which is part of the fuel electrode. As a result, Pt degrades if it has a contact with Ni, as shown in [49,50]. To measure polarization curves and EIS spectra, an electric load and impedance analyzer from BioLogic (SP-150 and booster VMP3B-80) is used. The temperature of the cell is measured using twelve thermocouples of type N, which are placed in the ceramic cell housing. Six thermocouples are placed on the fuel electrode side and six thermocouples are placed at the air electrode side, see Fig. 1. In addition, the air and fuel in and outlet temperatures are monitored to guarantee a sufficient fuel and air pre-heating. The control thermocouple of the furnace, which is used to measure the operating temperature, is placed close to the ceramic cell housing. The heating elements of the furnace are controlled with a previously tuned PID controller and solid state relays. The used test rig and the ceramic cell housing are described in more detail in a previous work [30]. Before the start of the presented tests, the cell was reduced and operated with different H_2 and N_2 mixtures from 17 vol% H_2 to 100 vol% H_2 for about 142 h. Further, the cell was operated with a 50 vol% H_2 and 50 vol% H_2O reference composition. The EIS curves showed changes during the first 16 h of operation with the reference composition but the EIS curves did not show further changes until the start of the presented tests (43 h after switching to the reference composition).

2.2. Test procedure

To investigate the utilization process of methane, the focus was laid on the fuel electrode resulting in 34 tested operating points. We investigated 3 different operating temperatures (700 °C, 750 °C and 800 °C) and two different methane flow rates. Further, we applied six different carbon containing gas mixtures which are based on three different steam to carbon ratios (H_2O/C) for internal and external autothermal reforming conditions. Three gas mixtures simulate the external autothermal reforming conditions (Ext. 1 - 3 in Table 2). They are measured during previous reforming experiments [48] and are supplied to the cell as a mixture of gases. The other three gas mixtures (Int. 2, 1.5, 1 in Table 2) only consist of steam and methane for the purpose of direct internal steam reforming. We applied reference measurements with the reference gas composition (Ref. Comp. in Table 2), in regular intervals. The reference measurements are used to detect changes of the cell along the test procedure. It should be mentioned here that the operating conditions are not designed to obtain the maximum electrical power output but to study the effect of methane based gas compositions on the cell. The air volume flow was adapted to avoid high pressure differences across the cell and avoid air starvation (the oxygen utilization rate is always below 16.5%). For Ext. gas composition, the volume flows on fuel and air electrode side are equal, which leads to air-fuel equivalence ratios of about 1 to 1.1. Int. gas compositions have a set air volume flow to reach an air-fuel equivalence ratio of 1 for compositions with $\dot{n}_C = 0.021\ \frac{\mathrm{mol}}{\mathrm{min}}$.

The test procedure was chosen in a way to theoretically avoid carbon deposition at an early stage of the tests. To predict solid carbon deposition at the fuel electrode, chemical equilibrium calculations are used, as suggested in literature [51]. Since solid C deposition and Ni oxidation are of interest to define the test procedure, the results of the chemical equilibrium calculations are shown in a ternary diagram, see Figs. 2(a) and 2(b). Chemical equilibrium calculations are described in detail in a previous work [48]. The results shown in Fig. 2 reveal that internal steam reforming compositions are closer to solid carbon formation and conditions Int. 1 tend to solid C deposition at every chosen operation temperature. That is the case since the Ext. gas compositions are auto-thermally reformed to not add more external energy to the process and being able to compare the impact at the same energy input levels.

The results from Fig. 2 led to one test procedure for the tested cell, as displayed in Fig. 2(c). Fig. 2(c) shows, that at every operating temperature, the gas compositions Ext. were tested first and gas compositions which are close to the C deposition region were tested last. The reference measurements are denoted as, for example, Ref.$_{750,Ext.02}$. Here, 750 is the set operating temperature in °C, Ext. is the kind of reforming before the reference measurement and 02 is a continuous numbering. Reference measurements are always conducted by supplying the reference gas composition (Ref. Comp. in Table 2).

At each operating point (gas composition, molar carbon flow and operating temperature) and reference measurement shown in Fig. 2(c), polarization curve measurements and step-wise impedance measurements were conducted. Step-wise impedance measurements mean that the direct current (DC) applied to the cell is increased step-wise, see Table 3. At each DC level, the cell was operated till a steady state was reached (settled temperature and voltage). After reaching a steady state, EIS measurements are conducted applying the settings listed in Table 3.

After the test procedure, the fuel electrode and air electrode are flushed with 1.5 slpm N_2 each and cooled down to room temperature at 0.5 K min^{-1}.

2.3. Data post processing

Within this work, temperature distributions and results from the EIS measurements are shown. The temperature distribution of the fuel electrode is calculated by linear interpolation between six thermocouples placed in the ceramic housing along the cell, see Fig. 1. The shown temperatures of these six points are their mean value over time of the presented operating point at steady conditions. It should be mentioned, that a dampened temperature profile might be visible since the thermocouples are placed in the ceramic housing. Nevertheless, the measured temperature profiles still provide information about hot and cold spots at the fuel electrode. The EIS data are post processed to calculate the DRT spectra. The post processing of the EIS data contains of three main steps:

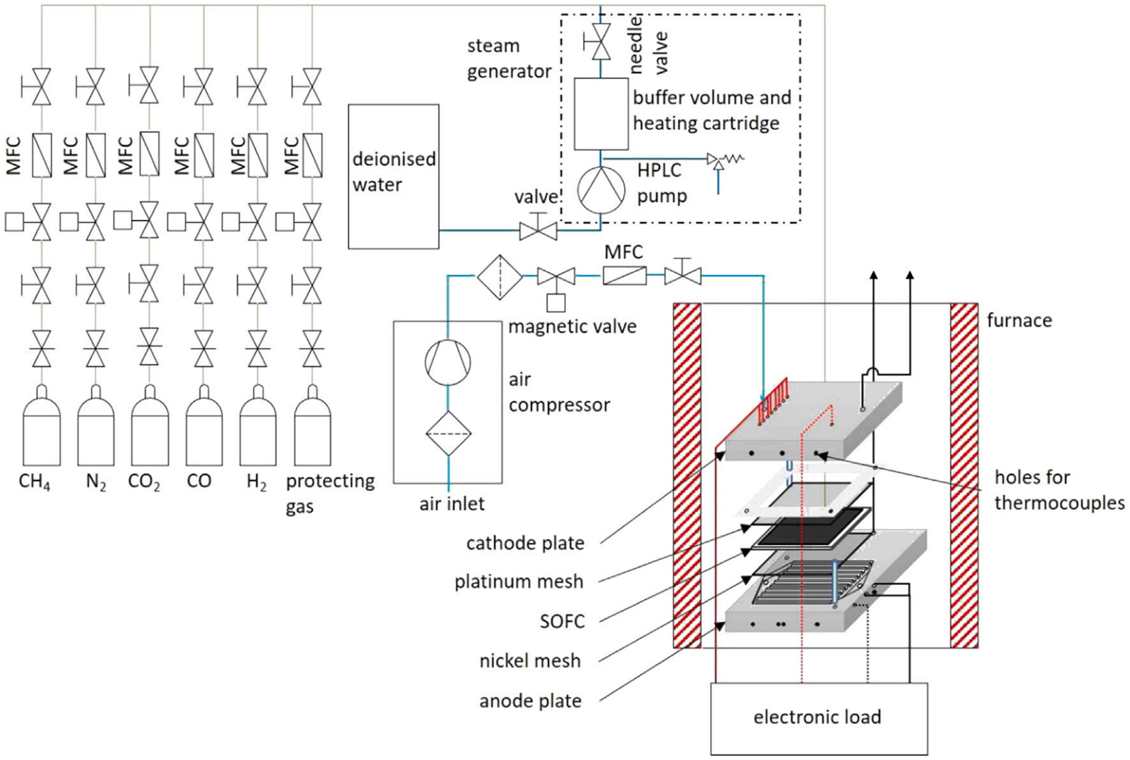

Fig. 1. Scheme of the used single cell test rig [30].

Table 2
Gas compositions at the cell inlet.

Name –	$\dot{n}_C$ in $\frac{\text{mol}}{\text{min}}$	n_{CH_4} in $\frac{\text{mol}}{\text{mol}_C}$	n_{H_2O} in $\frac{\text{mol}}{\text{mol}_C}$	n_{CO_2} in $\frac{\text{mol}}{\text{mol}_C}$	n_{H_2} in $\frac{\text{mol}}{\text{mol}_C}$	n_{CO} in $\frac{\text{mol}}{\text{mol}_C}$	n_{N_2} in $\frac{\text{mol}}{\text{mol}_C}$	$\dot{V}_{Air}$ slpm
Ext. 1a	0.021	0.140	0.671	0.482	1.652	0.378	2.780	2.873
Ext. 1b	0.042							5.747
Ext. 2a	0.021	0.135	0.870	0.549	1.682	0.316	2.896	3.035
Ext. 2b	0.042							6.07
Ext. 3a	0.021	0.130	1.085	0.601	1.679	0.270	3.051	3.208
Ext. 3b	0.042							6.417
Int. 1a	0.021	1.000	1.000	0.000	0.000	0.000	0.000	4.483
Int. 1b	0.042							
Int. 1.5a	0.021	1.000	1.500	0.000	0.000	0.000	0.000	4.483
Int. 1.5b	0.042							
Int. 2a	0.021	1.000	2.000	0.000	0.000	0.000	0.000	4.483
Int. 2b	0.042							
Ref. Comp.		H_2 = 1.25 slpm			H_2O = 1.25 slpm			2.500

Table 3
Settings for the EIS measurements.

Mode	DC	Alternating current (AC) amplitude	Lowest frequency	Highest frequency	Measuring points per decade
–	mA cm^{-2}	% of DC	Hz	Hz	–
Galvanostatic single sine	50, 100, 150, $150 + 100i$ ($i \in \mathbb{N} \mid 1 \ldots n$, n is limited by the lower voltage limit of 0.7 V)	4	10^{-1}	10^{5}	10

1. Filter the raw measurement data by dropping data points which have a deviation of more than 5% from the Kramers–Kronig test. [52]
2. Optimize the DRT parameters by reducing the deviation between the filtered impedance spectra and the impedance spectra recalculated from the DRT spectra.
3. Calculate the final DRT spectra with optimized DRT parameters and recalculate the EIS spectra from their final DRT spectra.

Applying the DRT method on measurement data which was filtered using the Kramers–Kronig test can lead to problems if there are only a few measurement points within the set limit of the Kramers–Kronig test. This issue can lead to a blurry DRT spectra. The same problem has

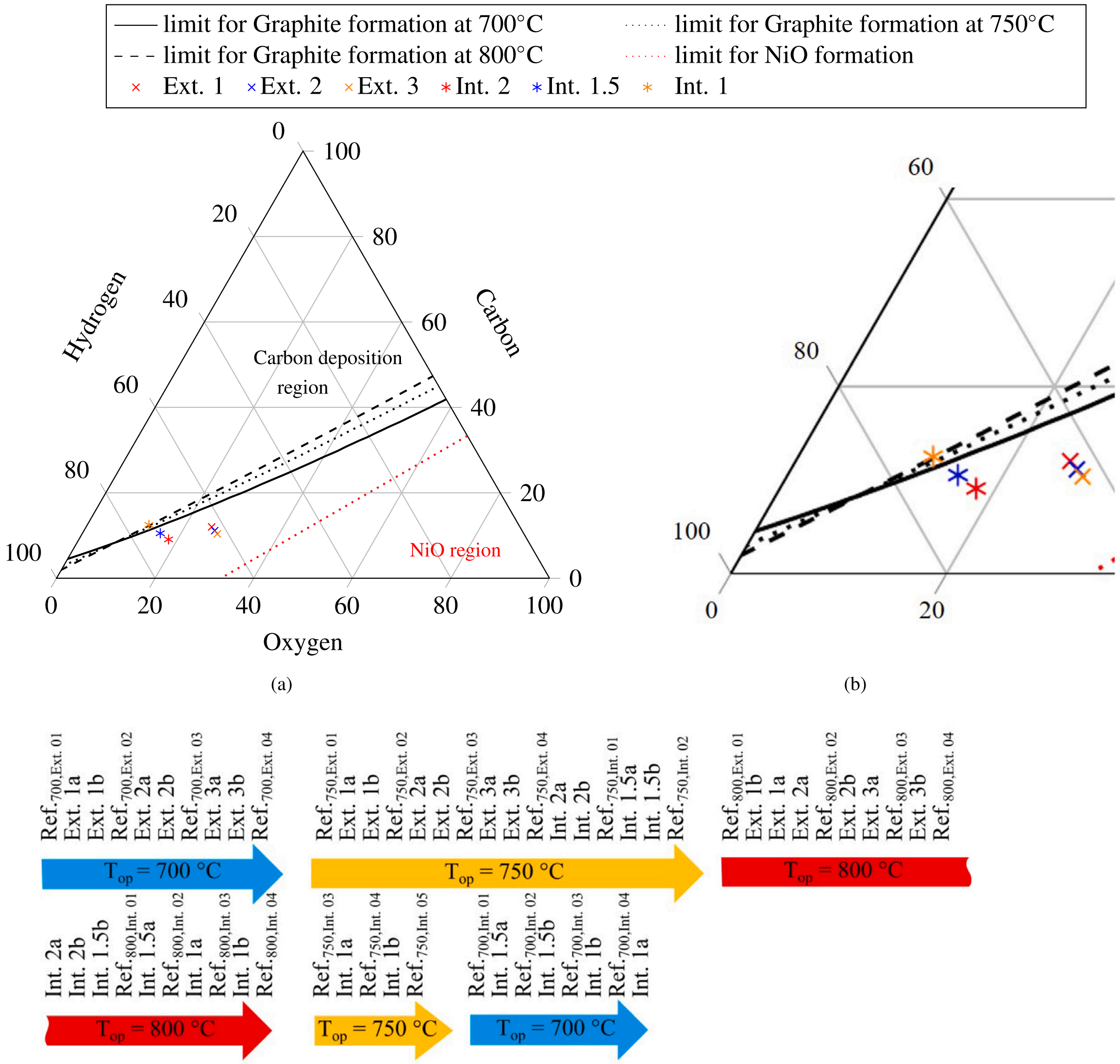

(a)

(b)

(c)

Fig. 2. (a) calculated C-H-O ternary diagram and (b) detail view of the area where the tested gas compositions are located and (c) the test procedure over time.

to be taken into account if non DRT based equivalent circuits are used to fit the impedance data.

3. Results and discussion

The following section shows results obtained during this work. The first part provides the overview of the cell behavior along the test procedure. The second part is about the post mortem analysis of the cell to identify possible degradation mechanisms which occurred during operation. The cells temperature distributions for different gas mixtures and fuel flows are shown in the third part. Finally, all previous results and an intensive literature study is considered to interpret the results from the I-V and EIS measurements which are shown in the fourth and fifth part of this section.

3.1. Test procedure

Within this section, the average, local minimum and maximum cell temperatures, the ohmic resistance at 100 mA cm^{-2} and the power output of the ASC at 0.7 V is given for each operating point (gas composition, molar carbon flow and operating temperature). The overview of the characteristic values (average cell temperature, ohmic resistance and power output), see Fig. 3, makes it possible to identify first tendencies of the cell behavior caused by different reforming conditions. Furthermore, the impact of the reforming conditions on the cell performance can be seen by observing the tendencies of the characteristic values of the reference measurements.

In Fig. 3(a), the average cell temperatures at 100 mA cm^{-2} and error bars that show the minimum and maximum measured local temperatures are shown along the operating time. The average cell temperature of all 12 thermocouples placed in the ceramic cell housing show only small differences between the reference measurements (maximum deviation of the average temperature is 5 K at T_{OP} = 700 °C, 4 K at T_{OP} = 750 °C and 3 K at T_{OP} = 800 °C). The average cell temperature of the Ext. gas compositions shows nearly the same values as for the reference composition. This might be the case since Ext. gas compositions contain more than 7 times less methane than comparable Int. gas compositions, leading to a lower impact of the endothermal reforming reactions. The cooling of the average cell temperature caused by the steam reforming reaction is clearly visible for all Int. gas compositions. No clear difference of the average cell temperature can be found between different H_2O/C ratios but a reduced average cell

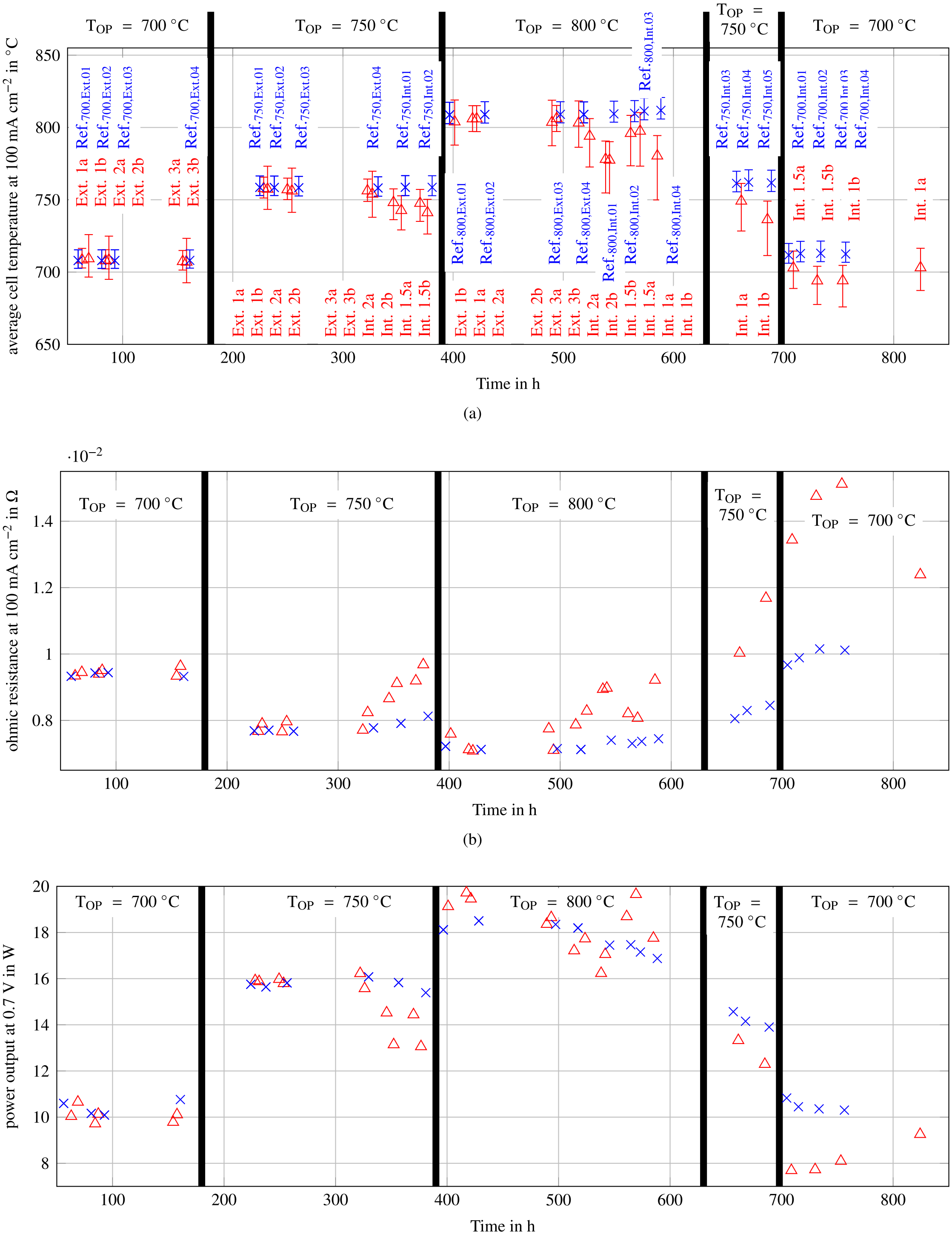

(a)

(b)

(c)

Fig. 3. Overview of the (a) average cell temperature with minimum and maximum measured local temperature, (b) ohmic resistance and (c) power output at 0.7 V for all operating points (△) and their reference measurements (×).

temperature is observed for increased methane flow rates. Furthermore, higher methane flow rate also show a higher temperature difference along the cell. In Fig. 3(a), the highest temperature difference of 44 K along the cell is found for Int. 1b at T_{OP} = 800 °C, which leads to a measured gradient of around 8.8 K cm^{-1}. Compared to that, the highest temperature difference with Ext. compositions is 32 K for Ext. 3b at T_{OP} = 800 °C and for Ref. Comp. the temperature differences along the cell are between 13 K and 15 K.

The ohmic resistance is shown in Fig. 3(b). It correlates with the average cell temperature due to the temperature dependency of the ion conduction in the electrolyte. In addition, two further effects seem to influence the ohmic resistance. First, it is observed that higher volume flows of the carbon containing gas mixtures lead to higher ohmic resistances. The increase in ohmic resistance due to the increased volume flows is likely caused by a decreasing local minimum cell temperature as due to a more dominant endothermal steam reforming reaction. The second effect that increases the ohmic resistance seems to be the H_2O/C ratio for internal reforming conditions at an operating temperature of 750 °C. The second effect is also observed for higher methane flows ($\dot{n}_C = 0.042 \frac{mol_C}{min}$) at all operating temperatures. The ohmic resistance of the reference measurements also changes along the testing time. Besides the change caused by different operating temperatures, the ohmic resistance of the reference measurements seem to increase after the cell was operated under direct internal reforming conditions while no changes were observed for external autothermal reforming conditions.

The power output of the cell at 0.7 V is shown in Fig. 3(c) and seems to correlate with the ohmic resistance. No performance increase was observed by increasing the fuel flow rate which might be caused by general low fuel utilization rates (up to ˜ 16%). The power output of the cell operated with external reformed methane is mostly higher or at least in the same range of direct internal reforming. This is the case even so, external reforming is done in autothermal mode. Latter means that parts of the initial methane flow, which is the same for both reforming types, is oxidized in the reformer. Hence, less oxidizable media is present at the cell during operation with external reformed methane but similar power outputs are achieved. The cooling of the cell due to direct internal steam reforming and the overall low fuel utilization rates are likely the cause of similar power outputs for both reforming types. The change in performance is discussed in more detail in 3.5. The performance loss of the cell observed through the decreasing power output of the reference measurements correlates with the changing ohmic resistance.

3.2. *Post mortem analysis*

Within the post mortem analysis, we performed scanning electron microscopy (SEM), Raman spectroscopy and energy dispersive x-ray spectroscopy (EDS) on several points across the cell on the substrate surface facing the gas compartment. The results gave us an idea of possible degradation mechanisms and changes of the cells microstructure that occurred during testing.

The results of EDS at three points (average of an area of 0.6×1 mm^2) along the cell are shown in Fig. 4. The EDS spectra were obtained by scanning areas at the gas and air inlet area of the cell, at the center of the cell and at the gas and air outlet area of the cell, see Fig. 4(a). The cracks that are visible in the cell typically occur during the cool down process in N_2 atmosphere and extraction of the cell from the ceramic housing. Fig. 4(c) shows the EDS spectra of the fuel electrode for the three points along the cell. Additionally to Ni, Y, Zr and O, which are part of the electrode material, a small C peak was detected. The Raman analysis of 4 areas with a size of 100×100 μm^2 for each investigated location (gas inlet area, center of the cell and gas outlet area) on the cell showed no C formation. Only SEM images and local EDS show some C deposition along the whole cell. Hence, the amount of deposited C might be quite small.

To better identify Ni oxidation through EDS, the surface on the Ni-mesh which is faced to the fuel electrode is analyzed at the same areas as the fuel electrode. The Ni-mesh is used as current collector at the fuel electrode side. We observed that the highest amount of Ni oxide on the surface of the Ni-mesh is present at the gas inlet area of the cell and the lowest amount of Ni oxide is present at the gas outlet area, see Fig. 4(d). Latter is also visible by SEM imaging. The SEM images revealed that contacting points between the electrode and the Ni-mesh seem to be homogeneous and clearly visible along the cell. Solid C deposition on the Ni-mesh is mainly found at the contacting points between the Ni-mesh and the fuel electrode. This was identified during the SEM scanning process of the Ni-mesh. Further, we found impurities (Al and Si), which might originate from the Ni-mesh since they were mainly found on the Ni grain boundaries during SEM scanning. The Al and Si impurities could also origin from contamination during the cell implementation with insulation material or from the steam supply. During the SEM scanning, a growth of the impurities on the Ni-mesh was observed from the gas inlet to the center of the cell. We also found indication for recrystallization of the Ni-mesh at the gas outlet area of the cell during the SEM analysis. The agglomeration and recrystallization could be an indication for a temperature gradient along the cell during operation.

The EDS spectra of the air electrode are shown in Fig. 4(e) for the sake of completeness. The overall composition of the air electrode does not seem to change along the cell. The only element which was found and is not part of the air electrode was solid C. We found solid C on the electrodes surface especially along the visible marks of the Pt-mesh on the air electrode. Hence we assume, that C might have deposited there during the cool down procedure where C, which was deposited on the fuel electrode side, was flushed from the fuel electrode side through cracks of the sealing or cell to the air electrode side. The cracks within the sealing and the cell typically occur during cool down of the cell in N_2 atmosphere. Therefore, EDS does not show degradation of the air electrode but the SEM images show degradation phenomena such as cathode delamination and cracks within the air electrode, see Fig. 4(b). The circular island formations of the electrode material as seen in Fig. 4(b) are found everywhere along the air electrode. They seem to already exist before the cell was implemented in the test rig, since the air electrode of the new cell also showed some island shaped structures. Investigation of several of these formations lead to the assumption that they are the starting points of cracks and sometimes even delamination and spalling of the air electrode are observed close to them, see Fig. 4(b). Beneath the spallings, the GDC barrier layer is visible, which was confirmed with EDS. Further, it seemed, that there are height differences of the surface which were found while scanning over the cell samples during SEM investigations. That leads to the conclusion that there might be an adhesion problem between the air electrode (LSCF) and the barrier layer (GDC).

3.3. *Temperature distribution*

The temperature deviation of tested gas compositions compared to their reference measurement are shown in Fig. 5. Only the temperature difference is shown to exclude effects caused by the long operation period and thermal cycling. Moreover, the influence of chemical reactions on the temperature distribution caused by CH_4 reforming are more apparent.

In Figs. 5(a)–5(c), three operating points with gas composition Ext. 03 are shown as a representative for all Ext. gas compositions. In Section 3.1, it was shown that the average cell temperatures of the Ext. gas compositions were nearly constant for all operating temperatures respectively. However, the ohmic resistance of Ext. gas compositions increased with increasing fuel flows. As shown in Figs. 5(a) and 5(b), the temperature difference between Ext. 06a and Ref. Comp. is nearly not existent, maximum temperature deviation is 4 K at $T_{OP} = 750$ °C and 6 K at $T_{OP} = 800$ °C. In Fig. 5(c) (higher methane flow rate), a temperature deviation of 17 K is visible at the central fuel inlet area. The cooler area at the cell inlet is correlated with the endothermal steam reforming reaction. Even so, the cooling at the gas inlet is visible in the temperature distribution its impact on the average cell temperature compared to the reference measurement is only about 6 K. However, the temperature gradient or its cause (the endothermal steam reforming reaction), could still be an explanation for the increased ohmic resistance as observed in Section 3.1. A more detailed discussion of the change of the ohmic resistance is provided in Section 3.5. An increased ohmic resistance was also observed for direct internal reforming of methane on disk cells with a diameter of up to 60 mm [10] and for the endothermal decomposition of ammonia on large planar cells with 80 cm^2 active area [53]. An increasing ohmic resistance as observed and the measured temperature distribution would lead to the assumption that the highest current density can be found at the cell inlet. However, a study found the highest local current density in the

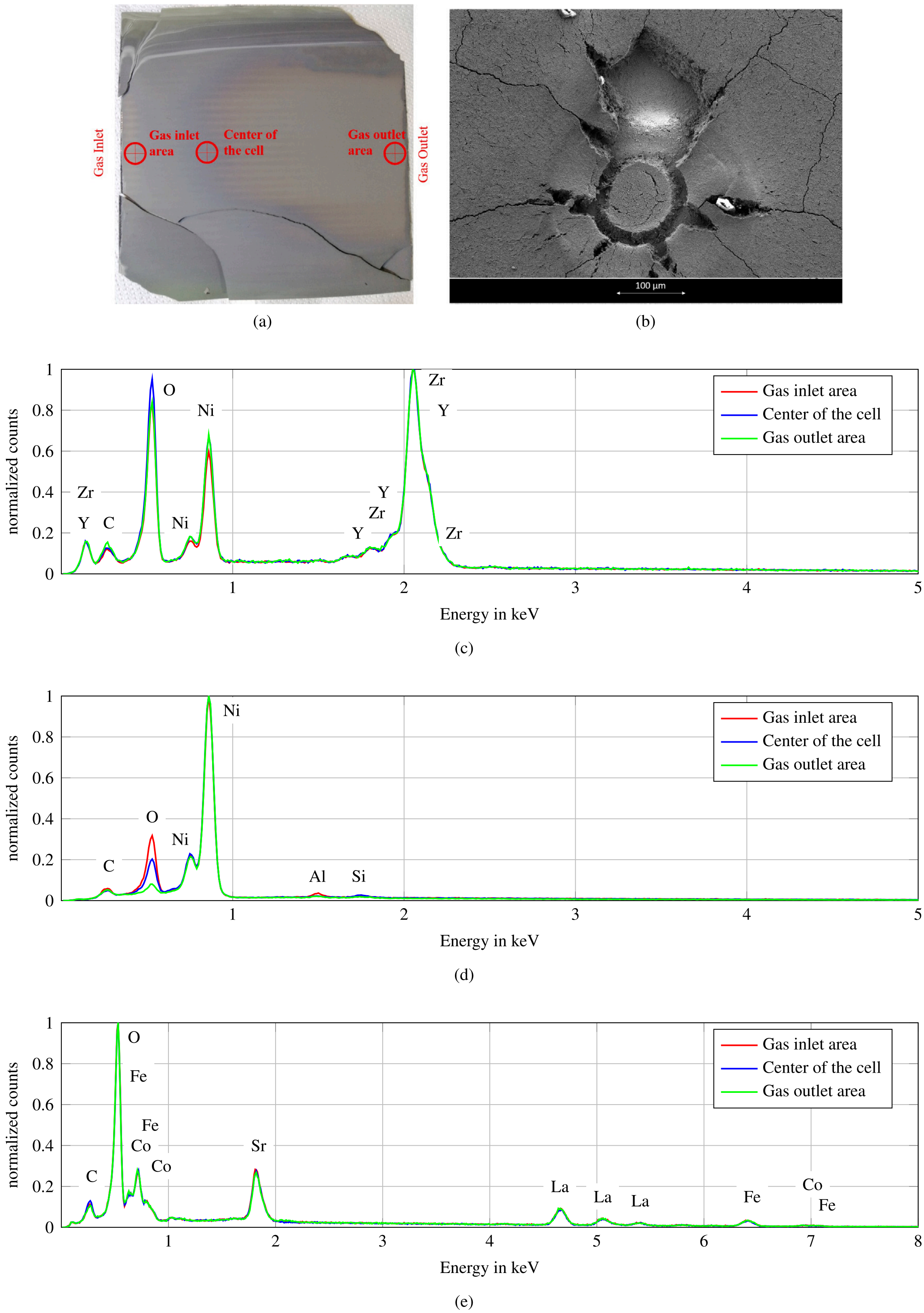

(a)

(b)

(c)

(d)

(e)

Fig. 4. (a) investigated areas of the cell, (b) SEM image of cathode delamination and cracking at the center area of the cell. EDS of the (c) fuel electrode, (d) Ni-mesh of the fuel electrode and (e) air electrode.

downstream half of a hydrogen operated SOFC [54]. Possible reasons for the correlation of increasing ohmic resistances and the more dominant steam reforming reaction in the temperature distribution are the change in cell temperature and blocking of the triple phase boundary by internal reforming reaction which reduces the electrochemical active cell area. Furthermore, we found that even if the CH_4 content of the gas mixtures is the same, the absolute flow rate of methane influences the temperature gradients and along the cell.

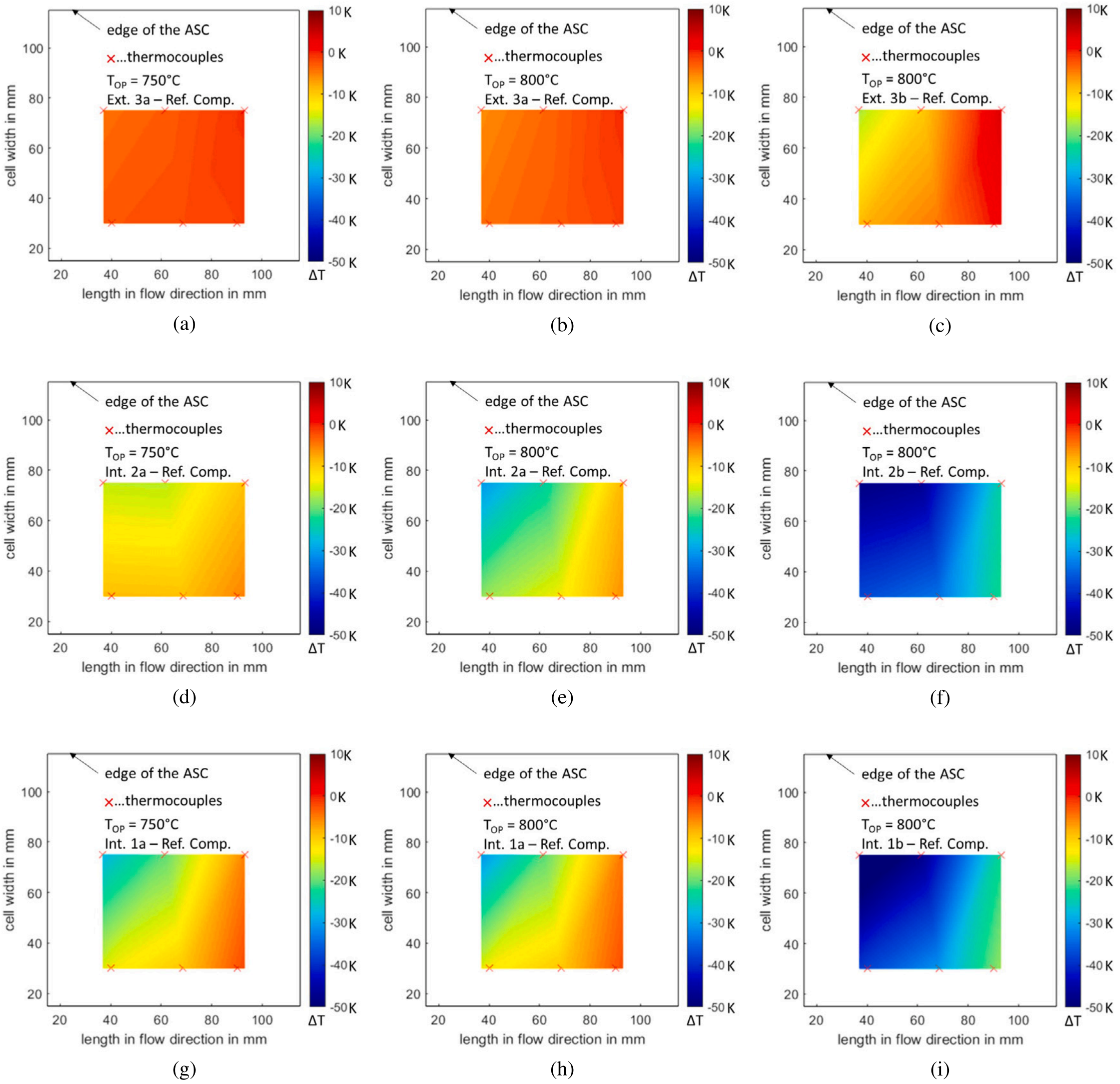

(a) (b) (c)

(d) (e) (f)

(g) (h) (i)

Fig. 5. Measured temperature profiles as temperature difference between tested reforming conditions and their respective reference measurement (Ref. Comp.) at 100 mA cm^{-2}. The abbreviations including the gas composition in (a) - (i), e.g. Ext. 3a - Ref. Comp., indicate the gas composition for which the temperature difference is shown (e.g. Ext. 3a - Ref. Comp.: temperature difference of the gas composition Ext. 3a and the respective reference measurement.).

Comparing the same fuel flows and gas compositions at different operating temperatures in Fig. 5, indicates that smaller temperature gradients are present if the operating temperature is lower. This trend is especially visible for direct internal reforming conditions. It also seems like the influence of the operating temperature on the temperature gradient increases with increasing H_2O/C ratio for direct internal reforming conditions. Therefore, the difference of the temperature gradient between Figs. 5(d) and 5(e) is higher compared to the difference between Figs. 5(g) and 5(h). This phenomenon might be explained by the following. Within this study, the flow rate of methane is held constant (at two different levels) which results in an increased fuel gas flow rate for an increased H_2O/C ratio. At higher fuel flow rates, the dwell time of the gas at the catalytic active surface is reduced. Further, the reaction kinetics are slower at lower operating temperatures. This could lead to more homogeneous distribution of endothermal methane reforming reactions along the cell at lower operating temperatures which is visible in a more homogeneous temperature distribution in Fig. 5(d) compared to Fig. 5(e) or Fig. 5(g). Comparing Fig. 5(d) to 5(f) with 5(g) to 5(i) respectively reveals that lower H_2O/C ratios lead to higher relative temperature gradients along the cell. For lower H_2O/C ratios, the temperature measured by the thermocouples at the gas outlet area of the cell is closer to the temperature of the respective reference measurement. The temperature measured at the gas inlet area of the cell is closer to the temperature of the respective reference measurement for higher H_2O/C ratios except for Fig. 5(e), which has nearly the same temperature difference at the gas inlet area as Fig. 5(h).

Concluding the findings in this section, it seems to be that external methane reforming reduces thermal stresses which might increase the lifetime of the SOFC. Further, if direct internal steam reforming is applied, lower operating temperatures in combination with high H_2O/C ratios seem to reduce thermal stresses while lower operating temperatures reduce the power output of the cell, see Fig. 3(c). It should be mentioned here, that high steam to carbon ratios could lead to Ni re-oxidation if high current densities or low fuel flow rates are applied [9,55]. The main reaction zone of the endothermal steam reforming reaction is observed at the central gas inlet area of the cell which applies thermal stresses at this location to the sealing and the cell itself.

3.4. Electrochemical characterization based on the reference gas composition

The operating points (gas composition, molar carbon flow and operating temperature) are characterized electrochemically by measurements of the polarization curves and EIS measurements with DRT

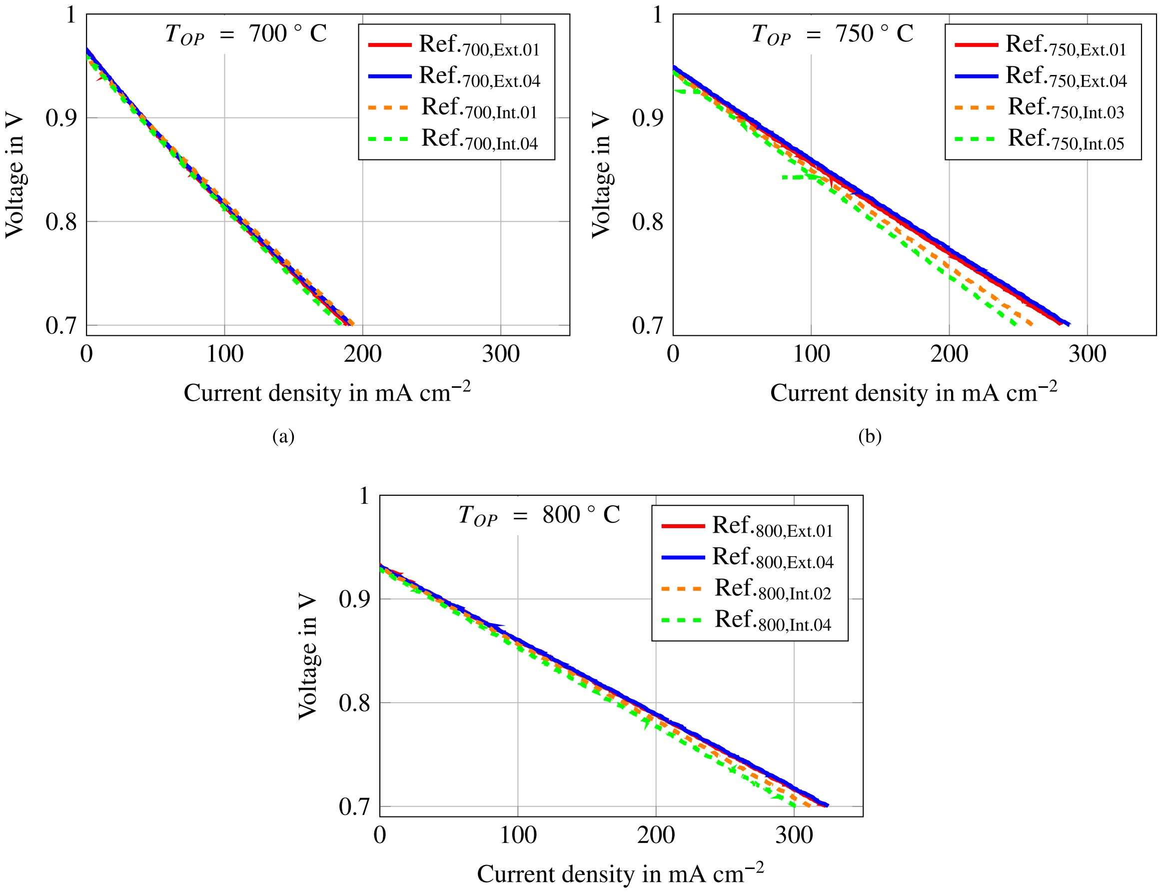

(a) (b)

(c)

Fig. 6. I-V curves of reference measurements at an operating temperature of (a) 700 °C, (b) 750 °C and (c) 800 °C, (—) at the beginning of testing, (—) after testing externally reformed gas compositions, (- - -) after testing the first internal reformed gas compositions and (- - -) at the end of testing at the respective operating temperature. (For interpretation of the references to color in this figure legend, the reader is referred to the web version of this article.)

analysis. In this section, measurements with the reference gas composition (Ref. Comp.) will be used to identify changes within the cell along the testing procedure.

In Fig. 6, I-V curves of the reference measurements (—) at the beginning of testing at the respective operating temperatures (700 °C, 750 °C and 800 °C), (—) after testing externally reformed gas compositions, (- - -) after testing the first internal reformed gas compositions and (- - -) at the end of testing at the respective operating temperature are shown. At every operating temperature, the same trend is observed. Testing externally reformed gas compositions lead to nearly no changes but a performance deterioration is observed during operation under direct internal reforming conditions, see Fig. 6. The largest performance loss is observed at 750 °C and the smallest is observed at 700 °C, even so Ref.$_{700,\mathrm{Ext.01}}$ (T_{OP} = 700 °C) was the first measurement and Ref.$_{700,\mathrm{Int.04}}$ (T_{OP} = 700 °C) was the last measurement of the presented test procedure.

To find the cause of the performance deterioration, EIS measurements at 100 mA cm^{-2} are compared in Fig. 7. Taking a look at Fig. 7 shows that several changes of the cell characteristic are taking place at different operating temperatures. In the following, the changes of the cell at each operating temperature as well as a comparison between the different operation temperatures will be discussed. To link the changes of EIS and DRT spectra with possible causes, a literature review, results from microscopic post mortem analysis and the temperature distributions will be used.

Results of EIS measurements and DRT analysis at an operating temperature of 700 °C are shown in Figs. 7(a) and 7(b) respectively. The EIS and DRT spectra show a significant change of the cell characteristic between Ref.$_{700,\mathrm{Ext.04}}$ and Ref.$_{700,\mathrm{Int.01}}$. The source of losses shifted from more dominant high frequency losses at the beginning of the test procedure to more dominant low frequency losses at the end of the test procedure. The Nyquist plot (Fig. 7(a)) shows also an increase of the ohmic resistance and the low frequency losses during direct internal reforming conditions (Ref.$_{700,\mathrm{Int.01}}$ to Ref.$_{700,\mathrm{Int.04}}$). Operating the cell at 700 °C revealed no changes between the two EIS spectra measured before and after operation with external reformed methane (Ref.$_{700,\mathrm{Ext.01}}$ and Ref.$_{700,\mathrm{Ext.04}}$). However, the EIS spectra between the reference measurement done before changing the operation temperature (Ref.$_{700,\mathrm{Ext.04}}$) and after changing the operation temperature back to 700 °C (Ref.$_{700,\mathrm{Int.01}}$) show a completely changed cell characteristic. This change might be caused by changing operating temperatures and applied carbon containing gas mixtures (Int. and Ext.). A more detailed analysis of the changes of the losses observed in the Nyquist plot is done by applying the DRT method.

In general, the resulting DRT spectra in Fig. 7 show four peaks, the low frequency peak (P_{LF}), the medium low frequency peak (P_{MLF}), the medium high frequency peak (P_{MHF}) and the high frequency peak (P_{HF}). The peaks which are illustrated with a dashed line are not considered for interpretation since the recalculation from DRT to EIS revealed that these peaks seem not to represent the measured impedance spectra within the measured range. However, having a closer look at the DRT spectra at an operation temperature of 700 °C shows that both low frequency peaks increase from reference measurement 04 to reference measurement 22. Further, P_{MLF} increases during operation at direct internal reforming conditions. Contrary to the low frequency peaks, the high frequency peaks (P_{MHF} and P_{HF}) decrease from reference

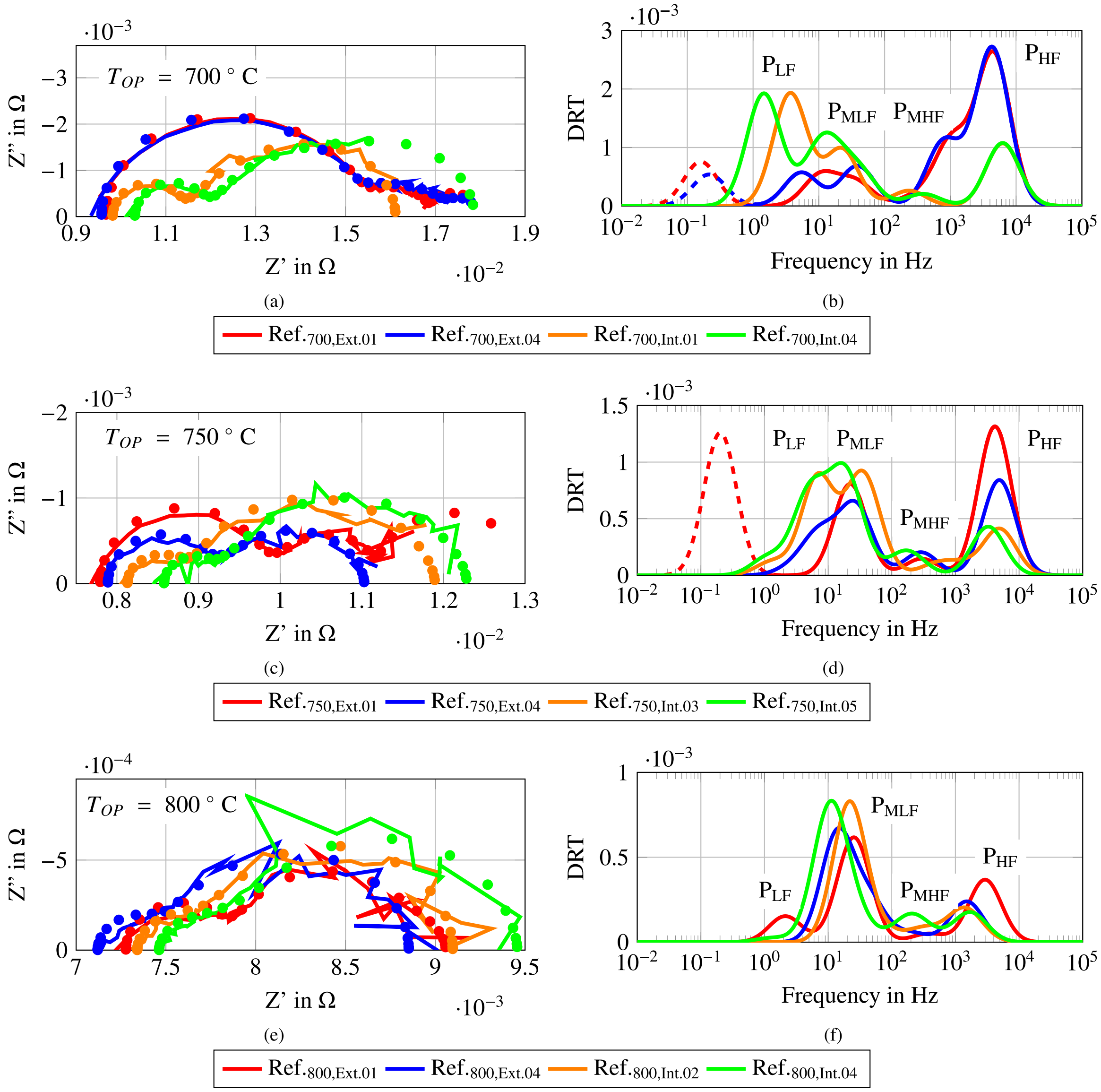

Fig. 7. (a), (c) and (e) show Nyquist plots of (–) measured EIS and (∘) from DRT recalculated EIS. (b), (d) and (e) show the DRT spectra at 100 mA cm^{-2}. The presented spectra are from the same reference measurements as presented in Fig. 6.

measurement 04 to reference measurement 22 but do not show changes between reference measurement 01 and 04 and reference measurement 22 and 25, see Fig. 7(b). As already observed in the Nyquist plot, the high frequency losses (P_{MHF} and P_{HF}) only change during operation at higher operating temperatures.

Figs. 7(c) and 7(d) show EIS and DRT spectra of the reference measurements at T_{OP} = 750 °C. Operation with carbon containing gas mixtures at 750 °C lead to an increase of the ohmic resistance, a decrease of the high frequency losses and an increase of the low frequency losses along the operation time, see Fig. 7(c). Even so, an increase of the ohmic resistance is observed between all reference measurements, the increase seems to be higher if the cell is operated under direct internal reforming conditions ($Ref._{750,Int.03}$ to $Ref._{750,Int.05}$) compared to operation with externally reformed methane ($Ref._{750,Ext.01}$ to $Ref._{750,Ext.04}$). The carried out DRT analysis in Fig. 7(d) shows more continuous changes of the high and low frequency losses compared to operation at 700 °C (Fig. 7(b)). For operation at 750 °C it is observed, that P_{HF} decreases when the cell is fueled with externally reformed methane ($Ref._{750,Ext.01}$ to $Ref._{750,Ext.04}$) and during operation at 800 °C ($Ref._{750,Ext.04}$ to $Ref._{750,Int.03}$). P_{HF}, however, does not change when the cell is operated under direct internal reforming conditions and after operation at 800 °C ($Ref._{750,Int.03}$ to $Ref._{750,Int.05}$). P_{MHF} does not seem to change according to a trend between all measurements conducted at 750 °C. However, the low frequency peaks (P_{MLF} and P_{LF}) are not clearly separated in Fig. 7(d) but it seems that P_{MLF} and P_{LF} increase especially during operation at 800 °C, this is visible if $Ref._{750,Ext.01}$ and $Ref._{750,Ext.04}$ are compared with Ref. Comp. $Ref._{750,Int.03}$ and $Ref._{750,Int.05}$.

In Figs. 7(e) and 7(f), the reference measurements at an operating temperature of 800 °C are shown. The Nyquist plots in Fig. 7(e) show changes of the ohmic resistance. In the beginning, the ohmic resistance decreases while the cell is operated with external reformed methane ($Ref._{800,Ext.01}$ to $Ref._{800,Ext.04}$) and then increases for operation under direct internal reforming conditions ($Ref._{800,Ext.04}$ to $Ref._{800,Int.04}$). In addition, a slight increase of the low frequency losses along the testing procedure is visible. More details of changes of low and high frequency losses are found in the DRT spectra (Fig. 7(f)). The DRT spectra shows a decrease of P_{HF} for operation with externally reformed methane ($Ref._{800,Ext.01}$ to $Ref._{800,Ext.04}$) and only a slight decrease for operation under direct internal reforming conditions ($Ref._{800,Ext.04}$ to $Ref._{800,Int.04}$). It also seems like P_{MLF} increases during the whole time the cell is operated at 800 °C.

Table 4
Possible influences of the observed DRT peaks according to literature [29].

Peak	Frequency range	Possible influences
P_{LF}	$10^0–10^1$ Hz	1. O_2 surface exchange and diffusion processes in the air electrode [56–58] 2. Gas diffusion and gas conversion in the fuel electrode [25,56,59,60] 3. H_2O partial pressure on the fuel electrode [10,59] 4. Fuel flow variation or fuel starvation [10,59]
P_{MLF}	$10^1–10^2$ Hz	1. O_2 surface exchange and diffusion processes in the air electrode [56–58] 2. O_2 surface exchange kinetics and O^{2-} diffusivity in the air electrode bulk [25] 3. H_2O partial pressure on the fuel electrode [10,59] 4. Fuel flow variation or fuel starvation [10,59]
P_{MHF}	$10^2–10^3$ Hz	1. O_2 surface exchange kinetics and O^{2-} diffusivity in the air electrode bulk [25,61] 2. H_2O partial pressure on the fuel electrode [10,59] 3. Charge transfer and ionic conduction processes in the fuel electrode [56,58,61] 4. H_2 partial pressure [56] 5. Temperature dependency [10]
P_{HF}	$10^3–10^4$ Hz	1. Electron transfer between the air electrode and current collector [57] 2. Charge transfer and ionic conduction processes in the fuel electrode [56,58,61] 3. H_2 partial pressure [56] 4. Gas diffusion coupled with charge transfer and ionic transport in the fuel electrode functional layer [25] 5. Temperature dependency [10]

Comparing the EIS results of the reference measurements of each operating temperature, shown in Fig. 7, with each other reveals that changes of the ohmic resistance at $T_{OP} = 750$ °C and $T_{OP} = 800$ °C do not change the ohmic resistance at $T_{OP} = 700$ °C equally. It is visible, that the increase of the ohmic resistance at $T_{OP} = 700$ °C is lower than the sum of the increased ohmic resistances at $T_{OP} = 750$ °C and $T_{OP} = 800$ °C. We also observed that the shift from dominant low frequency losses to dominant high frequency losses is mainly observed at an operating temperature of 750 °C and above but is still visible after returning to $T_{OP} = 700$ °C.

To interpret the described phenomena observed in the Nyquist and DRT plots, a literature study was conducted and summarized in Table 4. Table 4 shows also impacts of H_2O partial pressure, fuel flow rate and H_2 partial pressure on the DRT peaks. Hence, it has to be considered that measurements shown in Fig. 7 are done at the same gas composition and flow rates (Ref. Comp.).

While testing the SOFC according to the testing procedure described in 2.2, we observed an increase of P_{LF} and P_{MLF} for the reference measurements, see Fig. 7. The increase of the low frequency losses could be caused by (i) O_2 surface exchange and diffusion processes in the air electrode [56–58], (ii) gas diffusion and gas conversion in the fuel electrode [25,56,59,60] and (iii) O_2 surface exchange kinetics and O^{2-} diffusivity in the electrode bulk [25,61]. We found local Ni oxidation and nearly not detectable solid C depositions during the post mortem microscopic analysis on the substrate surface, see Section 3.2. Both Ni oxidation and C deposition could cause a reduced gas diffusion in the fuel electrode [22,59]. In our case it seems unlikely that the rare C depositions disturb the diffusion processes. Another possible cause for the increase of the low frequency losses could be cracks and local delamination of the air electrode from the GDC interlayer which were also found during the post mortem microscopic analysis. The cracks and local delamination of the air electrode could affect the O^{2-} diffusivity in the air electrode, which might be observed as a change of P_{MLF}. Since the low frequency losses increase most during direct internal reforming conditions, it might be the case that high temperature gradients accelerate phenomena like the local delamination of the air electrode or cracking of the cell or sealing which could lead to a decreased H_2 partial pressure or Ni re-oxidation. Delamination or contact loss of an LSCF electrode from the GDC interlayer due to thermal cycling is also reported in literature [62,63]. In our study, it is very likely that the delamination process is not initiated but accelerated by the thermal cycling since some defects of the air electrode seemed to be visible even at an unused cell. Beyond that, the cracking of the cell and its sealing cannot be excluded. A simulation of large planar SOFC stacks also showed that corners of the cell and glass ceramic sealings are concentration points of thermal stresses [28].

In addition to the increase of low frequency losses, a decrease of high frequency losses was observed in Fig. 7. The decrease of P_{HF} and P_{MHF} could be caused by enhanced (i) charge transfer and ionic conduction processes in the fuel electrode [56,58,61], (ii) electron transfer between the air electrode and current collector [57], (iii) reaction at triple phase boundary including charge transfer reaction [25] and (iv) elevated temperatures [10]. The decrease of the high frequency peaks seem not only to be caused by elevated temperatures since the average cell temperatures vary within a range of less than 5 K for each operating temperature shown in Fig. 7. It might be possible, that higher operating temperatures (750 °C and 800 °C) or local heat spots could have led to a better electronic conduction between the electrodes and their current collector, which lead to a better overall conductivity. Further, micro-structural changes of the fuel electrode at elevated temperatures (> 700 °C) might permanently enhance the gas diffusion or electrochemical processes at the triple phase boundary. Latter could lead to the conclusion, that the reduction of P_{HF} and P_{MHF} might not be caused directly by the different kinds of CH_4 reforming but could also be caused by operating the cell with carbonaceous species which lead to structural changes for longer operating periods.

3.5. Electrochemical characterization based on methane containing gas compositions

In the following, a direct comparison of the losses of externally reformed methane and direct internal reforming of methane is done by investigation of the EIS and DRT spectra at 100 mA cm^{-2}. In Fig. 8, the EIS and DRT spectra of gas composition Ext. 3a, Ext. 3b, Int. 2a and Int. 2b at 750 °C are shown. Further, the EIS and DRT spectra of three reference measurements, before Ext. 3a, after Ext. 3b and after Int. 2b are shown to observe the changes of the cell under reference conditions; for more information about the described testing sequence see Fig. 3. The EIS and DRT spectra in Fig. 8 are presented in the same style as in Fig. 7. However, the reference measurements in Figs. 8(a) and 8(b) show the same trends as seen for the other reference measurements at 750 °C in Fig. 7. Hence they are not described here in detail but used as reference for the interpretation of the other EIS and DRT spectra in Fig. 8.

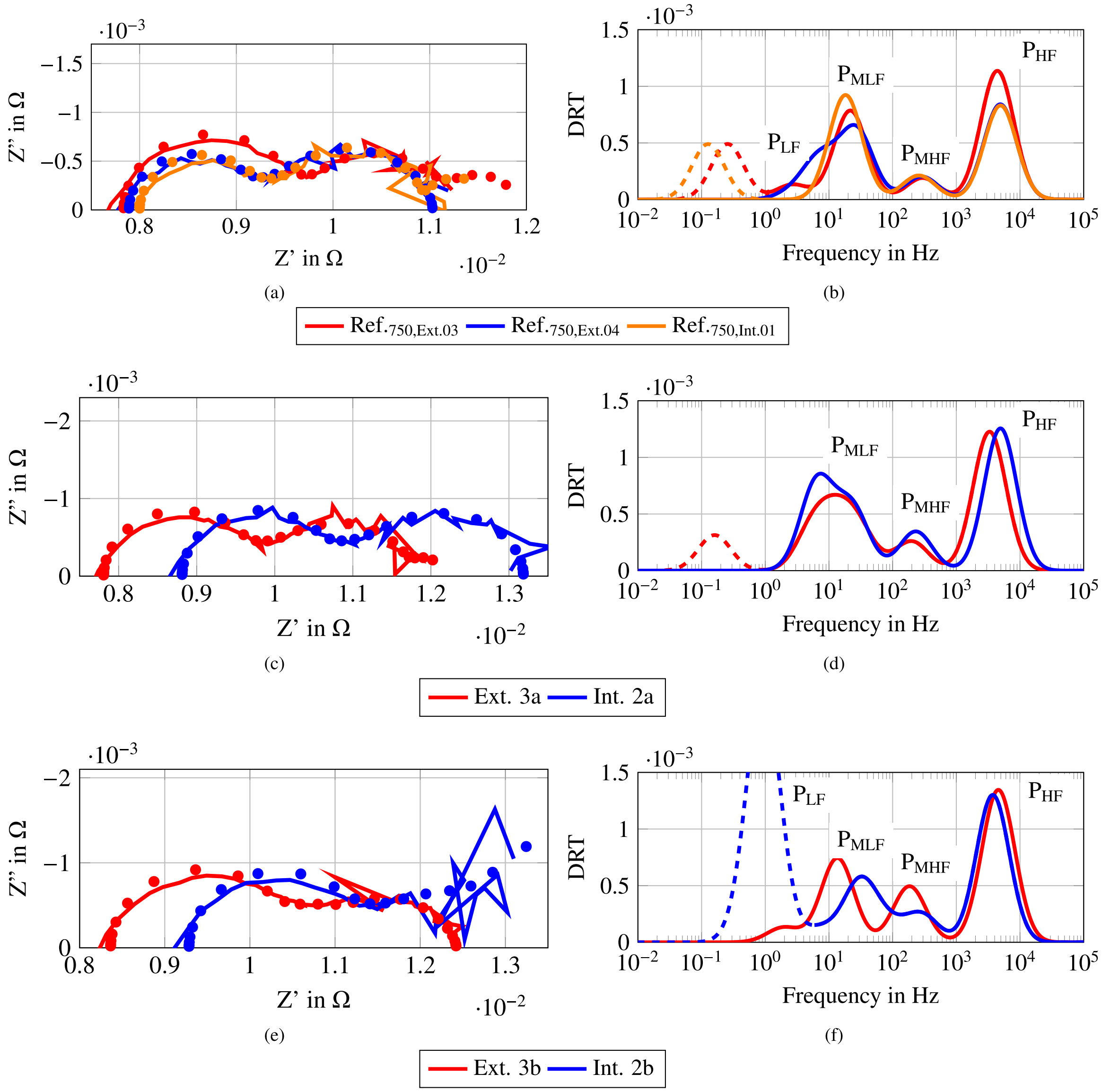

Fig. 8. Nyquist plots (a), (c) and (e) of (–) measured EIS, (o) from DRT recalculated EIS and DRT plots (b), (d) and (f) of direct internally (Int.) reformed methane, externally reformed (Ext.) methane and their surrounding reference measurements (Ref.$_{750,\mathrm{Ext.03}}$, Ref.$_{750,\mathrm{Ext.04}}$ and Ref.$_{750,\mathrm{Int.01}}$) at 750 °C and 100 mA cm^{-2}.

Figs. 8(c) and 8(d) show the Nyquist plot and DRT spectra of gas composition Ext. 3a and Int 2a. In Fig. 8(c) an increased ohmic resistance for Int. 2a compared to Ext. 3a is observed. The ohmic resistance of Ext. 3a is about the same size as from the reference measurements. This behavior fits with the presented temperature distribution in Fig. 5 and similar tests from literature [10]. The polarization resistance of Ext. 3a seems to be only slightly smaller than of Int. 2a but both are clearly higher compared to the reference measurement which could indicate CO oxidation as suggested in [10]. An increase of high frequency losses for methane compared to hydrogen was also observed in [64]. The DRT spectra of Ext. 3a and Int. 2a (Fig. 8(d)) differ only through slight changes of peaks P_{LF}, P_{MHF} and P_{HF}. All of these three peaks seem to be higher for direct internal reforming (Int. 2a) compared to external reforming (Ext. 3a). The peaks P_{LF} and P_{MHF} show the biggest difference in Fig. 8(d). The increase of P_{LF} could be due to deteriorated gas diffusion and conversion due to steam reforming reactions taking place at the fuel electrode. Another possibility is the degradation of the air electrode caused by cracking and local delamination, which might be accelerated by high temperature gradients as present during operation with Int. 2a. The degradation of the air electrode was observed in the post mortem microscopic analysis, see Section 3.2 and seems to have more impact than temporary deterioration of the gas diffusion in the fuel electrode. This suspicion is strengthened since changes are also visible between the reference measurements before and after Int. 2 (Ref.$_{750,\mathrm{Ext.04}}$ compared to Ref.$_{750,\mathrm{Int.01}}$). An only temporary change of the DRT spectra is observed for P_{MHF} in Fig. 8(d), since it does not appear in the reference measurements. The increase of P_{MHF} for Int. 2a could be caused by (i) deteriorated charge transfer and ionic conduction processes in the fuel electrode or (ii) increased steam and decreased H_2 partial pressure at the fuel electrode. Due to the different amounts of steam added and different reforming conditions, it seems likely that the higher amount of steam in Int. 2a compared to Ext. 1a might be at least part of the reason for the increase of P_{MHF} in Fig. 8(d) since it is observed several times in literature [10,56,59].

In Figs. 8(d) and 8(f), the height of P_{HF} does not seem to change much between Ext. and Int. but it changes between Ref.$_{750,\mathrm{Ext.03}}$ and Ref.$_{750,\mathrm{Ext.04}}$, see Fig. 8(b). According to literature, several processes are influencing P_{HF}. One explanation for a decrease of P_{HF} would be micro-structural changes of the fuel electrode leading to enhanced gas diffusion [25,58,65]. According to that, P_{HF} might not show a clear tendency comparing Figs. 8(d) and 8(f) due to the difference in the local gas composition at the cell. The different gas composition along the cell might cancel the reduction of P_{HF} caused by operation with Ext. 3, as seen from Ref.$_{750,Ext.03}$ to Ref.$_{750,Ext.04}$. Another explanation according to literature would be that P_{HF} is influenced by a combination of processes in the fuel electrode such as ionic transport, gas transport and the electrochemical oxidation [11,25]. These processes could be hindered by applying direct internal reforming conditions (Int.) due to the reforming reactions taking place at the fuel electrode and limit the available triple phase boundary. Latter would result in an increased P_{HF} if direct internal reforming conditions are applied.

In Figs. 8(e) and 8(f), the EIS and DRT spectra for Ext. 3b and Int. 2b (increased volume flow compared to Ext. 3a and Int. 2a) at 750 °C are shown. In Fig. 8(e) it is visible, that the ohmic resistance increased compared to Fig. 8(c). This might be caused by the more dominant cooling effect of the steam reforming reaction for higher volume flows, as shown in Fig. 5. Another reason for the increased ohmic resistance might be the methane reforming reactions which take place at the electrochemical active surface of the cell. The reforming reactions might reduce the available triple phase boundary by inhibiting electrochemical oxidation reactions. That might increase the ionic and electronic resistance which would lead to an increased ohmic resistance. A similar phenomenon was observed in literature for direct internal ammonia decomposition [53]. The polarization resistance of Ext. 3b seems to be qualitatively the same as for Ext. 3a, although the high frequency losses increased and the low frequency losses decreased comparing Ext. 3b with Ext. 3a. This difference is more clearly visible by comparing the DRT spectra from Figs. 8(d) and 8(e). The peaks P_{MHF} and P_{HF} are higher while the peak P_{MLF} occur thinner but at nearly the same height for Ext. 3b compared to Ext. 3a. The change of the peaks P_{MHF} and P_{HF} might be explained by an increase of reforming reactions taking place at the fuel electrode due to an increased methane flow. The reforming reactions might hinder the ionic transport, gas transport and / or the electrochemical oxidation process, as already assumed previously. The reduced width of peak P_{MLF} for Ext. 3b compared to Ext. 3a shows reduced losses in the low frequency range. The reduction of the low frequency losses might be caused by the increased fuel flow and air flow which might lead to enhanced O_2 surface exchange and diffusion processes in the air electrode. However, the Nyquist plot for Int. 2b in Fig. 8(e) shows the highest ohmic resistance in Fig. 8. It should be mentioned, that the highest methane flow rate is also present in Int. 2b which might follow the assumption that the cooling of the cell due to direct internal reforming and reforming reactions taking place at the fuel electrode hinder the electrochemical processes and increase the ohmic resistance. The low frequency losses of Int. 2b in Fig. 8(c) are not further used for interpretation since the direct internal reforming conditions were too unstable to obtain measurement results of a, for the authors, satisfying quality. Nevertheless, all shown data points within this work passed the Kramers–Kronig test and the DRT seems to fit the measured impedance quite well within the measured range. The DRT interpreted the low frequency losses as a large and dominant process (P_{LF}) which also influences the other peaks in Fig. 8(f).

4. Conclusion and outlook

Within this work, we performed electrochemical impedance spectroscopy, polarization curve measurements, spatially distributed temperature measurements and post mortem scanning electron microscopy, Raman shift spectroscopy and energy dispersive x-ray spectroscopy on the tested cell. All of these measurements are used to gain knowledge of the behavior of the cell during operation with carbonaceous gas mixtures and to interpret the EIS and DRT results. Thereby we were able to identify differences between internal and external methane reforming conditions within the EIS and DRT spectra related to the difference in temperature distribution or occurring reactions. One finding was a temporary increased ohmic resistance if the cell is operated under DIR conditions compared to external reformed methane and hydrogen steam mixtures. The increase of the ohmic resistance seems not only to be explainable by the lower average cell temperature but might be also caused by methane reforming reactions taking place at the electrochemical active area of the cell. We also found higher temperature gradients along the cell for DIR of methane compared to external reformed methane, which has similar temperature gradients as a hydrogen steam mixture. It seemed that the high temperature gradients caused by DIR might accelerate delamination of the LSCF air electrode from the GDC barrier layer if there are already inhomogeneities and cracks on the unused cell which do not cause degradation if the cell is operated with hydrogen or externally reformed gas mixtures. Hence, the integrity of the air electrode is a crucial factor not only for degradation stresses on the air side, but also for indirect thermal cycling caused by direct internal methane reforming. To confirm the findings within this work and show their applicability to larger SOFC stacks and systems, further tests should be carried out on the presented basis. The findings within this work contribute to the general knowledge of effects causing degradation of SOFCs and their impact on EIS and DRT spectra.

Applying the knowledge of the excessive and detailed planar single cell testing within this work on system level could lead to the conclusion that external methane reforming has a positive impact on planar cell degradation and process losses. Even if autothermal reforming is applied as external reforming type, the overall performance might be comparable to direct internal steam reforming if fuel utilization is not the limiting factor of the SOFC operation. This work also shows that if direct internal steam methane reforming is applied, higher steam to carbon ratios are favorable, not only because of a lower possibility of solid C deposition for higher steam to carbon ratios but also because of lower temperature gradients and reduced thermal stresses along the cell.

The following abbreviations are used in this manuscript:

AC	Alternating current
ASC	Anode supported cell
DC	Direct current
DIR	Direct internal reforming
DRT	Distribution of relaxation time
EDS	Energy dispersive x-ray spectroscopy
EIS	Electrochemical impedance spectroscopy
EU	European Union
GDC	Gadolinium doped ceria
H_2O/C	Steam to carbon ratio
LSCF	Lanthanum strontium cobalt ferrite
MFC	Mass flow controller
P_{HF}	high frequency peak
P_{LF}	low frequency peak
P_{MHF}	medium high frequency peak
P_{MLF}	medium low frequency peak
SEM	Scanning electron microscopy
slpm	standard litre per minute
SOFC	Solid oxide fuel cell
T_{OP}	operating temperature
YSZ	Yttria stabilized zirconia
Z	Impedance

CRediT authorship contribution statement

Michael Höber: Conceptualization, Methodology, Formal analysis, Investigation, Resources, Data curation, Writing – original draft, Visualization, Project administration. **Benjamin Königshofer:** Conceptualization, Investigation, Resources. **Hartmuth Schröttner:** Investigation, Data curation. **Harald Fitzek:** Investigation, Data curation. **Norbert H. Menzler:** Resources, Writing – review & editing. **Christoph Hochenauer:** Supervision, Project administration, Funding acquisition. **Vanja Subotić:** Conceptualization, Methodology, Resources, Writing – review & editing, Supervision, Project administration, Funding acquisition.

Declaration of competing interest

The authors declare that they have no known competing financial interests or personal relationships that could have appeared to influence the work reported in this paper.

Data availability

Data will be made available on request.

Acknowledgments

This project has been funded by partners of the ERA-Net SES 2018 joint call RegSys (www.eranet-smartenergysystems.eu) - a network of 30 national and regional RTD funding agencies of 23 European countries. As such, this project has received funding from the European Union's Horizon 2020 research and innovation programme under grant agreement no. 775970. The authors gratefully acknowledge the funding of this project entitled "AGRO-SOFC" (Grant No. 872299) by The Austrian Research Promotion Agency (FFG). We also want to mention that this work is done within the research initiative "Nachhaltige Personen- und Gütermobilität".

References

[1] European Environment Agency and Eurostat (aeiprghg), Agriculture-greenhouse gas emission statistics, Forschungsbericht, 2018, http://ec.europa.eu/eurostat/statisticsexplained/.

[2] Catello Pane, Giuseppe Celano, Alessandro Piccolo, Domenica Villecco, Riccardo Spaccini, Assunta M. Palese, Massimo Zaccardelli, Effects of on-farm composted tomato residues on soil biological activity and yields in a tomato cropping system, Chem. Biol. Technol. Agric. (ISSN: 2196-5641) 2 (1) (2015) 4, http://dx.doi.org/10.1186/s40538-014-0026-9.

[3] E. Dinuccio, P. Balsari, F. Gioelli, S. Menardo, Evaluation of the biogas productivity potential of some Italian agro-industrial biomasses, Bioresour. Technol. (ISSN: 09608524) 101 (10) (2010) 3780–3783, http://dx.doi.org/10.1016/J.BIORTECH.2009.12.113.

[4] Liyuan Fan, Chao'en Li, Purushothaman Vellayani Aravind, Weiwei Cai, Minfang Han, Nigel Brandon, Methane reforming in solid oxide fuel cells: Challenges and strategies, J. Power Sources (ISSN: 0378-7753) 538 (2022) 231573, http://dx.doi.org/10.1016/J.JPOWSOUR.2022.231573.

[5] C. Song, Fuel processing for low-temperature and high-temperature fuel cells challenges, and opportunities for sustainable development in the 21st century, Catal. Today (ISSN: 09205861) 77 (1–2) (2002) 17–49, http://dx.doi.org/10.1016/S0920-5861(02)00231-6.

[6] G. Pongratz, V. Subotić, H. Schroettner, B. Stoeckl, C. Hochenauer, A. Anca-Couce, R. Scharler, Investigation of solid oxide fuel cell operation with synthetic biomass gasification product gases as a basis for enhancing its performance, Biomass Convers. Biorefinery (ISSN: 21906823) 11 (1) (2021) 121–139, http://dx.doi.org/10.1007/s13399-020-00726-w.

[7] Valentina Somano, Domenico Ferrero, Massimo Santarelli, Davide Papurello, CFD model for tubular SOFC directly fed by biomass, Int. J. Hydrogen Energy (ISSN: 0360-3199) 46 (33) (2021) 17421–17434, http://dx.doi.org/10.1016/J.IJHYDENE.2021.02.147.

[8] María José Escudero, Conrado Valero, Miguel Angel Cauqui, Daniel Goma, María Pilar Yeste, Ni-Ce-ZrO2 system as anode material for direct internal reforming biogas solid oxide fuel cells, Fuel (ISSN: 00162361) 322 (2022) http://dx.doi.org/10.1016/J.FUEL.2022.124247.

[9] Hua Zhang, Wu Liu, Yuanhui Wang, Jianxin Wang, Jun Yang, Tongxiang Liang, Congling Yin, Bo Chi, Lichao Jia, Wanbing Guan, Performance and long-term durability of direct-methane flat-tube solid oxide fuel cells with symmetric double-sided cathodes, Int. J. Hydrogen Energy (ISSN: 03603199) 44 (54) (2019) 28947–28957, http://dx.doi.org/10.1016/j.ijhydene.2019.09.126.

[10] P. Caliandro, A. Nakajo, S. Diethelm, J. Van herle, Model-assisted identification of solid oxide cell elementary processes by electrochemical impedance spectroscopy measurements, J. Power Sources (ISSN: 03787753) 436 (2019) 226838, http://dx.doi.org/10.1016/j.jpowsour.2019.226838.

[11] Zewei Lyu, Hangyue Li, Minfang Han, Electrochemical properties and thermal neutral state of solid oxide fuel cells with direct internal reforming of methane, Int. J. Hydrogen Energy (ISSN: 03603199) 44 (23) (2019) 12151–12162, http://dx.doi.org/10.1016/j.ijhydene.2019.03.048.

[12] Mohammad Ali Abdelkareem, Waqas Hassan Tanveer, Enas Taha Sayed, M. El Haj Assad, Anis Allagui, S.W. Cha, On the technical challenges affecting the performance of direct internal reforming biogas solid oxide fuel cells, Renew. Sustain. Energy Rev. (ISSN: 18790690) 101 (2019) 361–375, http://dx.doi.org/10.1016/j.rser.2018.10.025.

[13] Andre Weber, Fuel flexibility of solid oxide fuel cells, Fuel Cells (ISSN: 1615-6846) (2021) http://dx.doi.org/10.1002/fuce.202100037, fuce.202100037.

[14] Vanja Subotić, Arianna Baldinelli, Linda Barelli, Robert Scharler, Gernot Pongratz, Christoph Hochenauer, Andrés Anca-Couce, Applicability of the SOFC technology for coupling with biomass-gasifier systems: Short- and long-term experimental study on SOFC performance and degradation behaviour, Appl. Energy (ISSN: 0306-2619) 256 (2019) 113904, http://dx.doi.org/10.1016/J.APENERGY.2019.113904.

[15] K. Girona, J. Laurencin, J. Fouletier, F. Lefebvre-Joud, Carbon deposition in CH4/CO2 operated SOFC: Simulation and experimentation studies, J. Power Sources (ISSN: 03787753) 210 (2012) 381–391, http://dx.doi.org/10.1016/j.jpowsour.2011.12.005.

[16] Bernhard Stoeckl, Vanja Subotić, Michael Preininger, Hartmuth Schroettner, Christoph Hochenauer, SOFC operation with carbon oxides: Experimental analysis of performance and degradation, Electrochim. Acta (ISSN: 00134686) 275 (2018) 256–264, http://dx.doi.org/10.1016/j.electacta.2018.04.036.

[17] J. Koh, Carbon deposition and cell performance of Ni-YSZ anode support SOFC with methane fuel, Solid State Ion. (ISSN: 01672738) 149 (3–4) (2002) 157–166, http://dx.doi.org/10.1016/S0167-2738(02)00243-6.

[18] Vanja Subotic, Philipp Harter, Bernhard Stoeckl, Michael Preininger, Michails Kusnezoff, Vincent Lawlor, Stefan Pofahl, Teko W. Napporn, Stefan Megel, Hartmuth Schroettner, Christoph Hochenauer, Fast fuel variation and identification of SOFC system changes using online health monitoring tools and fault diagnosis, ECS Trans. 91 (1) (2019) 753–759, http://dx.doi.org/10.1149/09101.0753ecst.

[19] Michael Geis, Stephan Herrmann, Sebastian Fendt, Hyeondeok Jeong, Christian Lenser, Norbert H. Menzler, Hartmut Spliethoff, Coupling SOFCs to biomass gasification - The influence of phenol on cell degradation in simulated bio-syngas. Part I: Electrochemical analysis, Int. J. Hydrogen Energy (ISSN: 03603199) 43 (45) (2018) 20417–20427, http://dx.doi.org/10.1016/j.ijhydene.2018.07.155.

[20] Hyeondeok Jeong, Michael Geis, Christian Lenser, Sandra Lobe, Stephan Herrmann, Sebastian Fendt, Norbert H. Menzler, Olivier Guillon, Coupling SOFCs to biomass gasification – the influence of phenol on cell degradation in simulated bio-syngas. Part II – Post-test analysis, Int. J. Hydrogen Energy (ISSN: 03603199) 43 (45) (2018) 20911–20920, http://dx.doi.org/10.1016/j.ijhydene.2018.09.006.

[21] H. Watanabe, R. Okino, K. Hanamura, Structural evolution of carbon deposition on a Ni/YSZ cermet of a SOFC analyzed by soft X-ray XANES spectroscopy, Int. J. Hydrogen Energy 44 (43) (2019) 24028–24035, http://dx.doi.org/10.1016/j.ijhydene.2019.07.122.

[22] Muhammad Shirjeel Khan, Seung-Bok Lee, Rak-Hyun Song, Jong-Won Lee, Tak-Hyoung Lim, Seok-Joo Park, Fundamental mechanisms involved in the degradation of nickel–yttria stabilized zirconia (Ni–YSZ) anode during solid oxide fuel cells operation: A review, Ceram. Int. (ISSN: 02728842) 42 (1) (2016) 35–48, http://dx.doi.org/10.1016/j.ceramint.2015.09.006.

[23] D. Sarantaridis, R.A. Rudkin, A. Atkinson, Oxidation failure modes of anode-supported solid oxide fuel cells, J. Power Sources (ISSN: 03787753) (2008) http://dx.doi.org/10.1016/j.jpowsour.2008.03.011.

[24] Antonin Faes, Aïcha Hessler-Wyser, Amédée Zryd, Jan Van herle, A review of RedOx cycling of solid oxide fuel cells anode, Membranes (ISSN: 2077-0375) 2 (3) (2012) 585–664, http://dx.doi.org/10.3390/membranes2030585.

[25] A. Kromp, S. Dierickx, A. Leonide, A. Weber, E. Ivers-Tiffée, Electrochemical analysis of sulfur-poisoning in anode supported SOFCs fuelled with a model reformate, J. Electrochem. Soc. (ISSN: 0013-4651) 159 (5) (2012) B597–B601, http://dx.doi.org/10.1149/2.015206jes.

[26] Jakub Kupecki, Davide Papurello, Andrea Lanzini, Yevgeniy Naumovich, Konrad Motylinski, Marcin Blesznowski, Massimo Santarelli, Numerical model of planar anode supported solid oxide fuel cell fed with fuel containing H2S operated in direct internal reforming mode (DIR-SOFC), Appl. Energy (ISSN: 03062619) 230 (2018) 1573–1584, http://dx.doi.org/10.1016/j.apenergy.2018.09.092.

[27] Yuhdai Kikuchi, Junko Matsuda, Yuya Tachikawa, Yusuke Shiratori, Shunsuke Taniguchi, Kazunari Sasaki, Degradation of SOFCs by various impurities: Impedance spectroscopy and microstructural analysis, ECS Trans. 78 (1) (2017) 1253–1260, http://dx.doi.org/10.1149/07801.1253ecst.

[28] Chih-Kuang Lin, Tsung-Ting Chen, An-Shin Chen, Yau-Pin Chyou, Lieh-Kwang Chiang, Finite element analysis of thermal stress distribution in planar SOFC, ECS Trans. 7 (1) (2007) 1977–1986, http://dx.doi.org/10.1149/1.2729310.

[29] Vanja Subotić, Christoph Hochenauer, Analysis of solid oxide fuel and electrolysis cells operated in a real-system environment: State-of-the-health diagnostic, failure modes, degradation mitigation and performance regeneration, Prog. Energy Combust. Sci. (ISSN: 0360-1285) 93 (2022) 101011, http://dx.doi.org/10.1016/J.PECS.2022.101011.

[30] Michael Höber, Benjamin Königshofer, Gernot Pongratz, Pavle Boškoski, Gjorgji Nusev, Christoph Hochenauer, Vanja Subotic, Experimental investigation of electrochemical reactions along SOFCs for internal and external reformed methane, ECS Trans. 103 (1) (2021) 2017–2031, http://dx.doi.org/10.1149/10301.2017ecst.

[31] Kazunari Sasaki, The impact of fuels on solid oxide fuel cell anode lifetime: The relationship between fuel composition, fuel impurities, and anode lifetime and reliability, in: Solid Oxide Fuel Cell Lifetime and Reliability: Critical Challenges in Fuel Cells, Elsevier Ltd, ISBN: 9780128097243, 2017, pp. 37–50, http://dx.doi.org/10.1016/B978-0-08-101102-7.00003-9.

[32] Bernhard Stoeckl, Vanja Subotić, David Reichholf, Hartmuth Schroettner, Christoph Hochenauer, Extensive analysis of large planar SOFC: Operation with humidified methane and carbon monoxide to examine carbon deposition based degradation, Electrochim. Acta (ISSN: 0013-4686) 256 (2017) 325–336, http://dx.doi.org/10.1016/J.ELECTACTA.2017.09.026.

[33] Zewei Lyu, Wangying Shi, Minfang Han, Electrochemical characteristics and carbon tolerance of solid oxide fuel cells with direct internal dry reforming of methane, Appl. Energy (ISSN: 03062619) 228 (2018) 556–567, http://dx.doi.org/10.1016/j.apenergy.2018.06.114.

[34] Vanja Subotić, Norbert H. Menzler, Vincent Lawlor, Qingping Fang, Stefan Pofahl, Philipp Harter, Hartmuth Schroettner, Christoph Hochenauer, On the origin of degradation in fuel cells and its fast identification by applying unconventional online-monitoring tools, Appl. Energy (ISSN: 03062619) 277 (2020) 115603, http://dx.doi.org/10.1016/j.apenergy.2020.115603.

[35] Vanja Subotić, Stefan Pofahl, Vincent Lawlor, Norbert H. Menzler, Thomas Thaller, Christoph Hochenauer, Online monitoring tools for SoH diagnostic and prognostic of remaining lifetime of reversible solid oxide cell (rSOC) systems, Energy Procedia (ISSN: 18766102) 158 (2019) 2329–2334, http://dx.doi.org/10.1016/j.egypro.2019.01.271.

[36] Ming Zhang, Yanshuo Liu, Dezhi Li, Xiaoli Cui, Licheng Wang, Liwei Li, Kai Wang, Electrochemical impedance spectroscopy: A new chapter in the fast and accurate estimation of the state of health for lithium-ion batteries, Energies (ISSN: 19961073) 16 (4) (2023) http://dx.doi.org/10.3390/en16041599.

[37] N. Müller, A. Jess, R. Moos, Direct detection of coke deposits on fixed bed catalysts by electrical sensors, Sensors Actuators B (ISSN: 09254005) 144 (2) (2010) 437–442, http://dx.doi.org/10.1016/j.snb.2009.03.008.

[38] N. Müller, C. Kern, R. Moos, A. Jess, Direct detection of coking and regeneration of single particles and fixed bed reactors by electrical sensors, Appl. Catal. A Gen. 382 (2) (2010) 254–262, http://dx.doi.org/10.1016/j.apcata.2010.05.001.

[39] N. Müller, R. Moos, A. Jess, In situ monitoring of coke deposits during coking and regeneration of solid catalysts by electrical impedance-based sensors, Chem. Eng. Process Technol. 33 (1) (2010) 103–112, http://dx.doi.org/10.1002/ceat.200900380.

[40] Michael Höber, Philipp Wachter, Benjamin Königshofer, Felix Mütter, Hartmuth Schröttner, Christoph Hochenauer, Vanja Subotić, In operando electrochemical impedance spectroscopy monitoring of nickel catalysts for hydrogen production, part I: Methodology and performance characterization, Fuel (ISSN: 00162361) 324 (2022) 124256, http://dx.doi.org/10.1016/j.fuel.2022.124256.

[41] Benjamin Königshofer, Michael Höber, Gjorgji Nusev, Pavle Boškoski, Christoph Hochenauer, Vanja Subotić, Accelerated degradation for solid oxide electrolysers: Analysis and prediction of performance for varying operating environments, J. Power Sources (ISSN: 03787753) 523 (2022) 230982, http://dx.doi.org/10.1016/j.jpowsour.2022.230982.

[42] Alexander Kromp, André Leonide, André Weber, Ellen Ivers-Tiffée, Hydrogen-oxidation kinetics in reformate-fuelled anode supported SOFC, ECS Trans. 35 (1) (2019) 665–678, http://dx.doi.org/10.1149/1.3570045.

[43] A. Thallam Thattai, L. van Biert, P.V. Aravind, On direct internal methane steam reforming kinetics in operating solid oxide fuel cells with nickel-ceria anodes, J. Power Sources (ISSN: 03787753) 370 (2017) 71–86, http://dx.doi.org/10.1016/J.JPOWSOUR.2017.09.082.

[44] Liyuan Fan, Chao'en Li, Lindert van Biert, Shou Han Zhou, Asif Nadeem Tabish, Anatoli Mokhov, Purushothaman Vellayani Aravind, Weiwei Cai, Advances on methane reforming in solid oxide fuel cells, Renew. Sustain. Energy Rev. (ISSN: 18790690) 166 (2022) http://dx.doi.org/10.1016/J.RSER.2022.112646.

[45] Yingtian Chi, Peiyang Li, Jin Lin, Jiarong Li, Shujun Mu, Yonghua Song, Fast and safe heating-up control of a planar solid oxide cell stack: A three-dimensional model-in-the-loop study, J. Power Sources (ISSN: 03787753) 560 (2023) 232655, http://dx.doi.org/10.1016/j.jpowsour.2023.232655.

[46] Qingping Fang, Norbert H. Menzler, Ludger Blum, Degradation analysis of long-term solid oxide fuel cell stacks with respect to chromium poisoning in La 0.58 Sr 0.4 Co 0.2 Fe 0.8 O 3-δ and La 0.6 Sr 0.4 CoO 3-δ Cathodes, J. Electrochem. Soc. (ISSN: 0013-4651) 168 (10) (2021) 104505, http://dx.doi.org/10.1149/1945-7111/AC2C11.

[47] Julian Szász, Florian Wankmüller, Virginia Wilde, Heike Störmer, Dagmar Gerthsen, Norbert H. Menzler, Ellen Ivers-Tiffée, Nature and functionality of La 0.58 Sr 0.4 Co 0.2 Fe 0.8 O 3-δ / Gd 0.2 Ce 0.8 O 2-δ / Y 0.16 Zr 0.84 O 2-δ interfaces in SOFCs, J. Electrochem. Soc. (ISSN: 0013-4651) 165 (10) (2018) F898–F906, http://dx.doi.org/10.1149/2.0031811jes.

[48] Michael Höber, Benjamin Königshofer, Philipp Wachter, Gjorgji Nusev, Pavle Boskoski, Christoph Hochenauer, Vanja Subotić, Holistic approach to design, test, and optimize stand-alone sofc-reformer systems, Processes (ISSN: 22279717) 9 (2) (2021) 1–28, http://dx.doi.org/10.3390/pr9020348.

[49] David F. Lupton, Jürgen Merker, Friedhold Schölz, The correct use of platinum in the XRF laboratorys, X-ray Spectrom. 26 (1997) 132–140, http://dx.doi.org/10.1002/(SICI)1097-4539(199705)26:3<132::AID-XRS223>3.0.CO;2-L.

[50] A.K.M.S. Chowdhury, S.A. Akbar, S. Kapileshwar, J.R. Schorr, A rugged oxygen gas sensor with solid reference for high temperature applications, J. Electrochem. Soc. (ISSN: 00134651) 148 (2) (2001) G91, http://dx.doi.org/10.1149/1.1343105.

[51] Tatsuya Takeguchi, Yukimune Kani, Tatsuya Yano, Ryuji Kikuchi, Koichi Eguchi, Keigo Tsujimoto, Yoshitaka Uchida, Akira Ueno, Koiji Omoshiki, Masanobu Aizawa, Study on steam reforming of CH4 and C2 hydrocarbons and carbon deposition on Ni-YSZ cermets, J. Power Sources (ISSN: 03787753) (2002) http://dx.doi.org/10.1016/S0378-7753(02)00471-8.

[52] Benjamin Königshofer, Pavle Boškoski, Gjorgji Nusev, Markus Koroschetz, Martin Hochfellner, Marcel Schwaiger, Đani Juričić, Christoph Hochenauer, Vanja Subotić, Performance assessment and evaluation of SOC stacks designed for application in a reversible operated 150 kW rSOC power plant, Appl. Energy (ISSN: 03062619) 283 (2021) 116372, http://dx.doi.org/10.1016/j.apenergy.2020.116372.

[53] B. Stoeckl, V. Subotić, M. Preininger, M. Schwaiger, N. Evic, H. Schroettner, C. Hochenauer, Characterization and performance evaluation of ammonia as fuel for solid oxide fuel cells with Ni/YSZ anodes, Electrochim. Acta 298 (2019) 874–883, http://dx.doi.org/10.1016/j.electacta.2018.12.065.

[54] C. Schluckner, V. Subotić, S. Preißl, C. Hochenauer, Numerical analysis of flow configurations and electrical contact positions in SOFC single cells and their impact on local effects, Int. J. Hydrogen Energy (ISSN: 03603199) 44 (3) (2019) 1877–1895, http://dx.doi.org/10.1016/J.IJHYDENE.2018.11.132.

[55] Muhammad Shirjeel Khan, Yohei Miura, Yosuke Fukuyama, Shuai Gao, Zhonghua Zhu, Methane internal steam reforming in solid oxide fuel cells at intermediate temperature, Int. J. Hydrogen Energy (ISSN: 03603199) 47 (29) (2022) 13969–13979, http://dx.doi.org/10.1016/J.IJHYDENE.2022.02.128.

[56] Hirofumi Sumi, Hiroyuki Shimada, Yuki Yamaguchi, Toshiaki Yamaguchi, Yoshinobu Fujishiro, Degradation evaluation by distribution of relaxation times analysis for microtubular solid oxide fuel cells, Electrochim. Acta (ISSN: 00134686) 339 (2020) 135913, http://dx.doi.org/10.1016/j.electacta.2020.135913.

[57] Mitra Ghamarinia, Alireza Babaei, Cyrus Zamani, Electrochemical characterization of La2NiO4-infiltrated La0.6Sr0.4Co0.2Fe0.8O3-δ by analysis of distribution of relaxation times, Electrochim. Acta (ISSN: 00134686) 353 (2020) 136520, http://dx.doi.org/10.1016/j.electacta.2020.136520.

[58] V. Sonn, A. Leonide, E. Ivers-Tiffée, Combined deconvolution and CNLS fitting approach applied on the impedance response of technical Ni8YSZ cermet electrodes, J. Electrochem. Soc. (ISSN: 00134651) 155 (7) (2008) B675, http://dx.doi.org/10.1149/1.2908860.

[59] Vanja Subotić, Bernhard Stoeckl, Vincent Lawlor, Johannes Strasser, Hartmuth Schroettner, Christoph Hochenauer, Towards a practical tool for online monitoring of solid oxide fuel cell operation: An experimental study and application of advanced data analysis approaches, Appl. Energy (ISSN: 03062619) 222 (2018) 748–761, http://dx.doi.org/10.1016/j.apenergy.2018.03.182.

[60] André Weber, Julian Szász, Sebastian Dierickx, Cornelia Endler-Schuck, Ellen Ivers-Tiffée, Accelerated lifetime tests for SOFCs, ECS Trans. 68 (1) (2015) 1953–1960, http://dx.doi.org/10.1149/06801.1953ecst.

[61] Qingping Fang, Ludger Blum, Norbert H. Menzler, Performance and degradation of solid oxide electrolysis cells in stack, ECS Trans. 68 (1) (2015) 3491–3503, http://dx.doi.org/10.1149/06801.3491ecst.

[62] Muhammad Zubair Khan, Muhammad Taqi Mehran, Rak Hyun Song, Seung Bok Lee, Tak Hyoung Lim, Effects of applied current density and thermal cycling on the degradation of a solid oxide fuel cell cathode, Int. J. Hydrogen Energy (ISSN: 0360-3199) 43 (27) (2018) 12346–12357, http://dx.doi.org/10.1016/J.IJHYDENE.2018.04.175.

[63] Wanbing Guan, Zhiguang Du, Jianxin Wang, Long Jiang, Jun Yang, Xiao-Dong Zhou, Mechanisms of performance degradation induced by thermal cycling in solid oxide fuel cell stacks with flat-tube anode-supported cells based on double-sided cathodes, Int. J. Hydrogen Energy (ISSN: 03603199) 45 (38) (2020) 19840–19846, http://dx.doi.org/10.1016/j.ijhydene.2020.05.114.

[64] Yuanbo Lin, Zhongliang Zhan, Jiang Liu, Scott A. Barnett, Direct operation of solid oxide fuel cells with methane fuel, Solid State Ion. (ISSN: 01672738) 176 (23–24) (2005) 1827–1835, http://dx.doi.org/10.1016/J.SSI.2005.05.008.

[65] A. Leonide, V. Sonn, A. Weber, E. Ivers-Tiffée, Evaluation and modeling of the cell resistance in anode-supported solid oxide fuel cells, J. Electrochem. Soc. (ISSN: 00134651) 155 (1) (2008) B36, http://dx.doi.org/10.1149/1.2801372.